Colloidal Cerium Oxide Nanoparticles: Synthesis and Characterization Techniques

Jamie C. Clinton

Thesis submitted to Virginia Polytechnic Institute and State University
Master of Science
Electrical Science and Engineering

Dr. Kathleen Meehan - Chair
Dr. Richey Davis
Dr. Masoud Agah

January 26, 2008
Blacksburg, Virginia

Keywords: Cerium Oxide, Optical Spectroscopy, Absorption, Fluorescence, Nanoparticle

Colloidal Cerium Oxide Nanoparticles:

Synthesis and Characterization Techniques

Jamie Clinton

Dr. Kathleen Meehan, Chair

Abstract

Fluorescence spectra and UV-Vis absorption spectra are collected on cerium oxide nanocrystalline particles. While CeO_2 is the stable form of bulk cerium oxide, ceria nanoparticles exhibit a nonstoichiometric composition, $CeO_{2-\gamma}$, due to the presence of oxygen vacancies and the formation of Ce_2O_3 at the grain boundaries. The Ce(III) ions, which are more reactive and therefore more desirable for various applications, are created by oxygen vacancies, which act as defects in the $CeO_{2-\gamma}$ crystal lattice. These defects form trap states in the band gap of CeO_2, which can be seen in the absorption spectra. Ce(III) is required for fluorescence of the ceria nanoparticles while Ce(IV) is involved in only nonradiative transitions. The optical spectroscopy results show that the ceria samples have different ratios of Ce(III) ions to Ce(IV) ions, which is verified by x-ray photoemission spectroscopy (XPS).

Acknowledgements

First of all, I would like to express my appreciation to my graduate advisor, Kathleen Meehan. The knowledge she imparted upon me was critical to this thesis being completed. I wish to thank Dr. Rick Davis for all his questions asked during our meetings, which helped to make this thesis as robust as possible. I would also like to thank Dr. Bev Rzigalinski for the use of her laboratory and her equipment. Thanks to Masoud Agah for being the final member of my defense committee.

I wish to thank Will Miles for taking the time to teaching me all the basics of surface chemistry. Also thanks to Will for all of the collaboration on this project. His assistance in data collection made the project much easier. I would also like to thank Neeraj Singh and Shaadi Elswaifi for the assistance in setting up and using their spectrometer.

Thanks to Frank Cromer for training me to use the XPS system and then helping me to analyze the data. Thanks to Dr. Steve McCartney for his help in obtaining TEM images. I appreciate the financial support received from the Virginia Tech Institute for Critical Technologies and Applied Science.

I would like to thank my parents for all their support and I am very thankful that they were always there for me. Last but not least, I would like to thank Jacqueline Esparza for having the everlasting patience to put up with me during all the stressful times that come with being a graduate student.

Table of Contents

List of Figures

List of Table

Chapter 1 Introduction

Cerium oxide (ceria) is a wide bandgap semiconductor that has long been known for its catalytic capabilities[1] and has been synthesized and studied in both thin-film[2,3] and nanoparticle form[4-6]. As a thin-film, cerium oxide has unique properties such as a high refractive index, a high dc dielectric constant and a lattice constant similar to Si, making it suitable as an insulating material in Si device technology[7]. These properties make cerium oxide useful for applications in microelectronics and optics.

Recently, ceria nanoparticles have attracted attention within the biomedical research community as a potential agent to inhibit cellular aging[8,9]. Mixed brain cell cultures have been shown to have an increased lifespan when a solution containing ceria nanoparticles is introduced into their environment. The likely mechanism for the longevity increase is the scavenging of free radical species in the cells that would normally damage the cell, causing the cell to age[10]. The scavenging effect is attributed to the presence of Ce(III) ions that reduce the free radical species as the Ce(III) ions are oxidized to Ce(IV).

In this study, seven cerium oxide colloidal samples are compared using various forms of spectroscopy. The main goal of the project was to find a way to determine the Ce(III) concentration in the ceria nanoparticles using optical spectroscopy. The optical spectroscopy techniques used were spectrophotometry, to measure the absorption spectrum of the samples, and fluorometry, to measure the fluorescence of the samples. These techniques are widely used to characterize semiconducting materials[11], but have not been extensively used on ceria nanoparticles. One advantage of these techniques is that the optical spectroscopy systems are inexpensive and have fast data acquisition.

Another advantage is that the samples can remain in their colloidal environment, thus maintaining the chemistry at the surface as the particles are characterized. X-ray photoemission spectroscopy (XPS) and Raman spectroscopy have previously been used to determine the concentration of Ce(III) and Ce(IV) in ceria[12-14]. However, both techniques have drawbacks, which prevent their use to monitor changes in these concentrations real-time under most experimental condition. XPS requires extensive sample preparation, including drying the sample, that may change the surface characteristics of the sample, and data acquisition is slow. A high power laser is required to perform Raman spectroscopy and requires an expensive high resolution monochromator to resolve the Stokes and anti-Stokes optical signals.

The catalytic activity of these samples has been measured previously[15]. In this study, a correlation between the absorption and the fluorescence spectra of the samples was found as well as a correlation between these optical properties and the sample's catalytic activity. The fluorescence spectrum was found to be a more sensitive measure than the absorption spectrum. The Ce(III) contribution to the absorption spectrum overlapped the Ce(IV) contribution and deconvolution was an issue. Experimental results of absorption and fluorescence spectroscopy were reinforced by XPS results that verified the conclusions drawn from absorption and fluorescence.

In order to accurately interpret the results of the optical spectroscopy techniques used, the theory behind fluorescence and absorption in semiconducting materials is given in Chapter 2 along with the theory behind light scattering and cellular longevity. In Chapter 3, all of the experimental procedures are given in detail. Chapter 4 presents the results and discussion of all the techniques used to analyze the ceria nanoparticles.

Results are given for spectrophotometry, fluorometry, X-Ray photoelectron spectroscopy (XPS) and X-Ray diffraction (XRD). Results are also given for the properties of the samples, including particle sizes determined from transmission electron microscopy (TEM), surface area measurements from performing Brunauer-Emmitt-Teller (BET) and size measurements from dynamic light scattering (DLS). Chapter 5 concludes with a recapitulation of the methods used and the results found and Chapter 6 presents ideas for future research.

Chapter 2 Background

2.1 Luminescence

Luminescence is the emission of photons from a material where the emission spectrum is not a function of the sample's temperature[16]. This occurs when an electron from an excited state relaxes to a lower state, releasing a photon in the process. The excitation can take place in numerous forms. If the electron is excited by an electrical current, it is called electroluminescence. Excitation by a chemical process is known as chemiluminescence. When the excitation takes place in mechanical form, it is mechanoluminescence. Photoluminescence is the process that occurs when photons are used as the excitation source for the electrons and occurs in two forms. The first form is phosphorescence. Phosphorescence occurs when photons continue to radiate long after the excitation has stopped due to the fact that the excited state has an extremely long lifetime, usually because the only transition down to the ground state is radiative and is a forbidden transition. The second form is fluorescence. Fluorescence occurs when an

electron is excited by an incoming light source (which is also true for phosphorescence). Photons are then emitted as the electrons return to the ground state. In fluorescence, as opposed to phosphorescence, the excited electrons stay in the upper energy band for a very short time, typical lifetimes are in the microsecond range or less, and to the human eye the sample would cease to fluoresce once the light source is terminated.

The incoming light, with photon energy hυ, will excite the electrons from a ground state E_1 to an upper energy level E_2. The photon energy hυ must be high enough to excite the electron from E_1 to E_2. If hυ is larger than E_2-E_1, the excess energy is released as heat. Figure 1 shows this schematically.

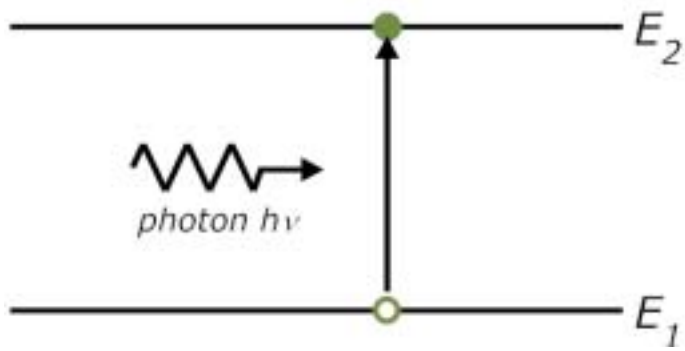

Figure 1. Schematic showing the absorption process.

The process of exciting an electron by a photon is known as absorption. Once the electron is in the higher energy state, one of two radiative processes can occur. First, the electron can relax back to the lower level E_1, releasing a photon after having stayed at the upper excited state E_2 for a certain amount of time. This is known as spontaneous emission and is shown in Figure 2. A photon emitted during spontaneous emission has a random phase and direction of propagation when compared to the photon that was absorbed to excite the electron.

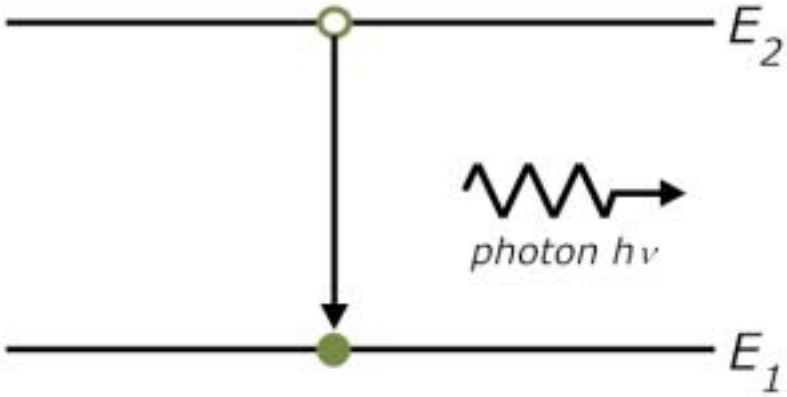

Figure 2. Schematic showing spontaneous emission.

The second radiative process occurs when the excited electron interacts with an incoming photon, causing the electron to release a photon with the same momentum and frequency as the incoming photon. This is known as stimulated emission and is shown in Figure 3.

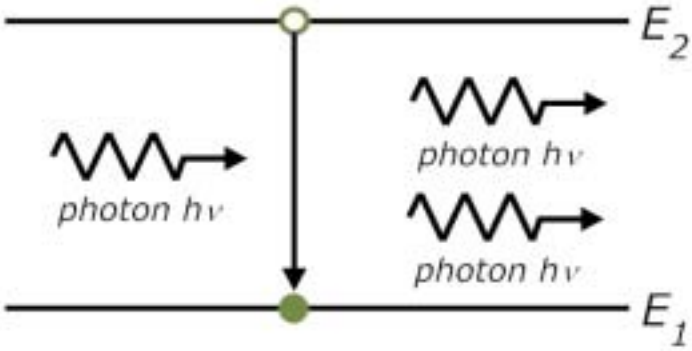

Figure 3. Schematic showing stimulated emission.

There are other possible non-radiative paths in a two-level system where the electron can relax that involve Auger recombination, phonon-electron interactions, or require other multi-particle combinations. These other transition can be ignored if the

radiative lifetime of the excited electron is short. Multi-particle transitions usually need to be taken into account if the radiative lifetime is long or there is a high concentration of these other particles.

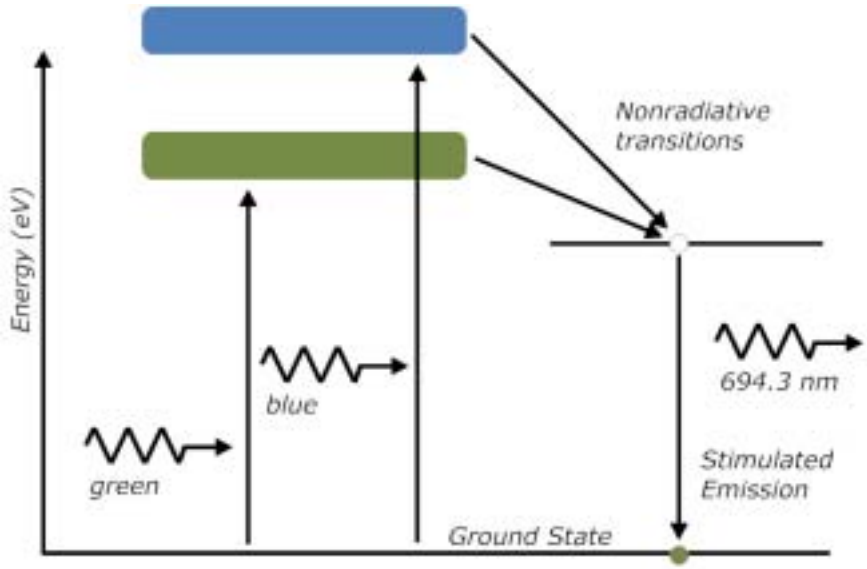

Figure 4. Processes that occur in a ruby laser.

Figure 4 [Redrawn from Ref. 18] shows a schematic of a more complicated system: the radiative and non-radiative paths of a ruby laser. This system has two excitation levels, with both relaxing to an intermediate level through a nonradiative process. Finally, the electrons in the intermediate level relax back to the ground state, releasing photons in the process. The photons released can either have a random momentum, caused by spontaneous emission, or the photon can be 'knocked out' by an incoming photon, resulting in two photons with matching momentum and frequency. In a bulk material where the photons are not confined and are allowed to leave the material without purposely being reflected back into the material, spontaneous emission dominates. This happens because only a small amount of photons are available to cause

stimulated emission due to the fact that most photons are emitted in a random direction and quickly exit the sample. When a structure is used to confine the photons, a buildup of photons with the same wavelength occurs and the likelihood that an excited electron relaxes via stimulated emission increases. The point at which the number of photons emitted by a material is generated equally by spontaneous and stimulated emission is known as the lasing threshold. A typical structure that is used to enable lasing is an etalon, where mirrors are used to keep the photons trapped in the material.

2.2 Einstein Coefficients

When an electron is excited, it will have some probability of relaxing on its own by spontaneous emission. This probability is given by the Einstein coefficient, A. A_{ij} is defined as the probability per second of a spontaneous jump from level i to level j[17]. If there are N_2 electrons per unit volume in the level 2, then

$$R_{spon}=N_2A_{21}. \qquad \text{Eq. 1}$$

where R_{spon} is the rate at which electrons will relax from level 2 to level 1 per second. For a system with no incoming radiation and an initial number of excited electrons, N_{2o}, the amount of excited electrons after time t will is given by

$$N_2(t) = N_{2o}e^{-A_{21}t}. \qquad \text{Eq. 2}$$

The time in which the population falls to 1/e of its initial value is called the natural lifetime of level 2, τ_2; where τ_2 is equal to $1/A_{21}$.

When an excited electron is stimulated by a photon to jump to a lower energy level, the photon emitted by the electron transition will be in phase with the incoming photon. The rate at which stimulated emission occurs is given as

$$R_{stim}=u_\nu N_2B_{21}, \qquad \text{Eq. 3}$$

where N_2 is the number of electrons per unit volume in the upper energy level, B_{21} is the probability per second of a stimulated jump from level 2 to level 1, and u_v is the spectral energy density of the incoming photons. B_{21} is associated with the jump from some energy level, 2, to a lower energy level, 1 and, hence, is the Einstein coefficient associated with stimulated emission. .

Electrons make an upward transition by absorbing a photon; this process is known as absorption. The rate of electrons leaving the lower energy level is

$$R_{abs}=u_v N_1 B_{12}. \qquad \text{Eq. 4}$$

The spectral energy density, u_v, is the same as before and N_1 is the number of electrons per unit volume in the lower energy level. B_{12} is the final Einstein coefficient, which governs the rate at which electrons are excited by incoming photons. It is not a coincidence that equations three and four appear similar; it can be shown that B_{12} is equal to B_{21}, and thus stimulated emission is the analogue of absorption. While the rate equations for stimulated emission and absorption are similar, there is no analogue for spontaneous emission. An electron cannot spontaneously jump to a higher energy level; energy for this jump must be provided through a transfer from one or more additional particles. One important property of equation one, three and four is that the rate of each process is proportional to the electron population density of the involved energy level.

Finally, it can be shown that there is a relationship between A and B[18]. The Einstein relations are:

$$B_{12}=B_{21} \qquad \text{Eq. 5}$$

and

$$\frac{A_{21}}{B_{21}}=\frac{8\pi h \upsilon^3}{c^3}, \qquad \text{Eq. 6}$$

where c is the speed of light, h is Planck's constant, and ν is the frequency of the photon emitted as a result of the electron's relaxation from level 2 to level 1. From this equation, it can be seen that the ratio of A_{21}/B_{21} increases with increasing frequency (and thus the energy) of the photon released. Therefore, spontaneous emission is expected to dominant in systems where there is little confinement of light, u_ν is small, and the energy of the emitted photon, $E_{photon} = h\nu = hc/\lambda$, is large.

2.3 Absorption

2.3.1 Direct Bandgap Absorption

To determine the absorption properties of a semiconducting material, the density of states (DOS), N(E), is important. The DOS represents the number of available states at an energy level per unit volume[16]. To determine the DOS, the semiconductor is assumed to have no quantum confinement; the electrons, with effective mass m^*, are free to move in three dimensions. The number of energy states between E and E + dE is then:

$$N(E)dE = \frac{1}{2\pi^2\hbar^3}(2m^*)^{3/2}\sqrt{E}dE \text{, for } E \geq 0. \qquad \text{Eq. 7}$$

Now consider Figure 5 [Redrawn from Ref. 15], showing the absorption of a photon between two direct valleys. Every initial state at E_i is associated with a final state E_f and for parabolic bands:

$$h\nu - E_g = \frac{\hbar^2 k^2}{2}\left(\frac{1}{m_e^*} + \frac{1}{m_h^*}\right). \qquad \text{Eq. 8}$$

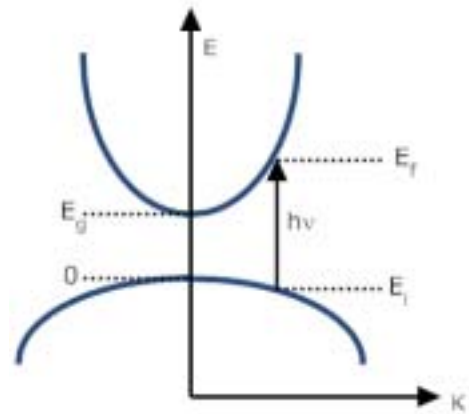

Figure 5. E-K diagram showing electron transition.

The effective mass of the electrons and holes are m_e^* and m_h^*, respectively. The density of directly associated states will then be found to be:

$$N(E) = \frac{8\pi\sqrt{2}}{h^3} m_r^{3/2} \sqrt{h\nu - E_g} \qquad \text{Eq. 9}$$

where the reduced effective mass is:

$$m_r = \frac{m_e^* m_h^*}{m_e^* + m_h^*} \qquad \text{Eq. 10}$$

where m_e^* is the effective mass of an electron at the bottom of the conduction band and m_h^* is the effective mass of a hole (a missing electron) at the top of the valence band.

The absorption coefficient is defined as the relative rate of decrease in light intensity L(hυ) along its propagation path:

$$\alpha = \frac{1}{L(h\nu)} \frac{d[L(h\nu)]}{dx} \qquad \text{Eq. 11}$$

and is expressed in units of cm^{-1}[16]. The absorption coefficient for a given photon energy hυ is proportional to the probability for the transition from the initial state to the

final state and also the density of available final states. This process must be summed for all possible transitions between states separated by an energy difference equal to hυ. The absorption equations shown here were assumed to have all lower states filled and all upper states empty. This is known as the low light condition where ρ(ν) is very small.

From equation eleven, it can be derived that the absorption coefficient for a direct bandgap semiconductor is

$$\alpha(h\nu) = A^*(h\nu - E_g)^{1/2}. \qquad \text{Eq. 12}$$

A* is constant for any given material and is given by

$$A^* = \frac{q^2\left(2\frac{m_h^* m_e^*}{m_h^* + m_e^*}\right)^{3/2}}{nch^2 m_e^*} \qquad \text{Eq. 13}$$

where q is the charge on an electron, n is the index of refraction and c is the speed of light[16].

2.3.2 Band Tailing

Knowing the DOS and carrier concentration is theoretically enough to plot the absorbance of a semiconductor. But there is a problem that occurs experimentally. Theory states that when $h\upsilon=E_g$, N(E)=0, but experimentally this rarely occurs[16]. Perturbations form in the DOS that extend into the conduction and valence bands, thus the DOS is nonzero extending into the bandgap. These perturbations are caused by impurities in the crystal. An ionized donor exerts an attractive force on the conduction electrons and a repulsive force on the valence holes. Acceptors act conversely, and since the impurities are distributed randomly within the crystal lattice, the local interaction will vary over the lattice as impurities cluster inhomogenously. Figure 6 [Redrawn from Ref.

15] shows local variances that may arise in the bandgap caused by impurities. Figure 7 [Redrawn from Ref. 15] shows the ideal DOS and a DOS with tails extending into the bandgap.

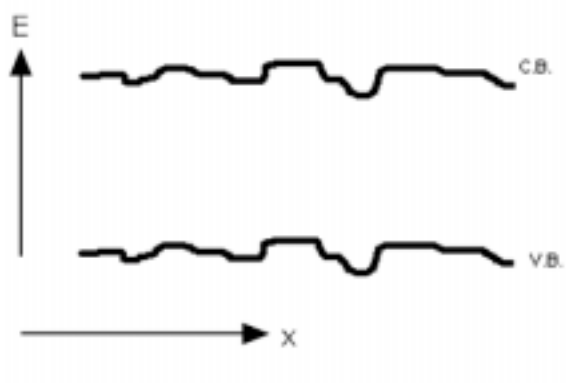

Figure 6. Band perturbations caused by impurities.

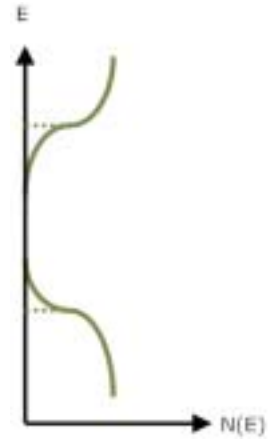

Figure 7. DOS when band perturbations are present. The dotted lines show the ideal DOS.

The local bandgap, E_c-E_v at any particular point, will always be constant. The perturbations arise due to the fact that the DOS distribution, which integrates the number of states at each energy level within the whole volume, sees that there are conduction band states at lower energies than E_c and valence band states at energies higher than E_v.

Band tails are important when measuring the absorption of a semiconducting material. Ideally, the material would not absorb below its bandgap, but band tails introduce states in the bandgap and absorption does occur below the bandgap. The tails are dependent on the amount of impurities and introduce a slight slope that changes the absorbance spectrum. Figure 8 [Redrawn from Ref. 15] shows the ideal absorbance spectrum for a direct bandgap semiconductor and an absorbance spectrum with DOS that extend into the bandgap.

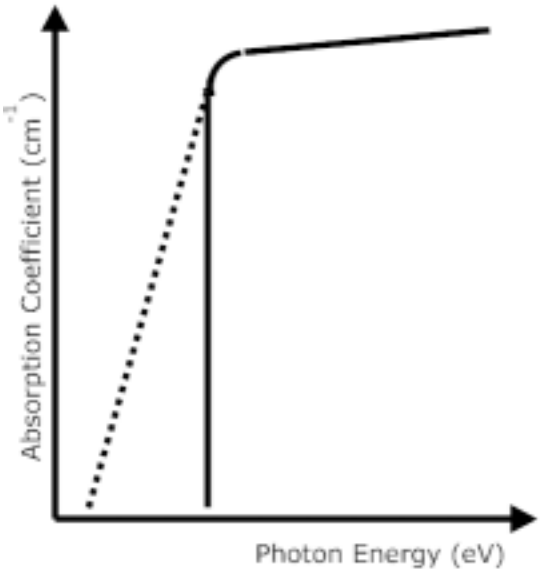

Figure 8. Band tailing that occurs during absorption when impurities are present.

When band tailing occurs, the slope of the absorption edge becomes

$$\frac{d(\ln\alpha)}{d(h\nu)} = \frac{1}{kT}. \qquad \text{Eq. 14}$$

This is known as Urbach's rule[16]. The absorption coefficient then is found to have two parts. The first part,

$$\alpha(h\nu)_I = A*(E - E_g)^{1/2}, \qquad \text{Eq. 15}$$

occurs above a certain crossover energy $\frac{kT}{2\sigma} + E_g$, and a second part,

$$\alpha(h\nu)_{II} = K_o \exp\left[\frac{\sigma}{kT}(E - E_g)\right], \qquad \text{Eq. 16}$$

occurs below the crossover energy. K_o is a scaling constant and σ is a phenomenological constant that determines the steepness of the absorption tail. The absorption tail at energies lower than E_g is called Urbach's tail and its steepness is an indicator of the

impurities in the semiconductor, where the smaller the slope of the tail, the higher the density of impurities present.

2.3.3 Indirect Bandgap Absorption

Although a photon with energy $h\upsilon > E_g$ is sufficient to excite an electron in a direct bandgap semiconductor, another step is required in an indirect semiconductor[16]. Here, the transition requires a change in momentum as well as a change in energy. Since the photon has insufficient momentum to adequately excite the electron in this case, a phonon is required to complete the transition while conserving energy in this process. A phonon is a quantum of mass vibration. Each phonon has an energy E_p and will be either emitted or absorbed in the transition. These two processes are given respectively by

$$h\upsilon_e = E_f - E_i + E_p \qquad \text{Eq. 17}$$

$$h\upsilon_a = E_f - E_i - E_p. \qquad \text{Eq. 18}$$

An absorption coefficient can be derived for each process.

$$\alpha_a(h\nu) = \frac{A(h\nu - E_g - E_p)^2}{\exp\left(\frac{E_p}{kT}\right) - 1} \qquad \text{Eq. 19}$$

and

$$\alpha_e(h\nu) = \frac{A(h\nu - E_g + E_p)^2}{1 - \exp\left(-\frac{E_p}{kT}\right)} \qquad \text{Eq. 20}$$

are the absorption coefficients where phonon absorption occurs and phonon emission occurs, respectively.

The total absorption coefficient is the sum of both possible transitions given as:

$$\alpha(h\nu) = \alpha_a(h\nu) + \alpha_e(h\nu).$$

Here $\alpha_a(h\upsilon)$ begins to absorb when $h\upsilon = E_g - E_p$ and $\alpha_e(h\upsilon)$ begins to absorb when $h\upsilon = E_g + E_p$. Since the denominator in α_e is larger than the denominator in α_a, α_e is much greater than α_a when $h\upsilon > E_g - E_p$. However α_a is responsible for all of the absorption in the window +/- E_p around E_g. No absorption takes place when $h\upsilon < E_g - E_p$. This is shown schematically in Figure 9 [Redrawn from Ref. 15].

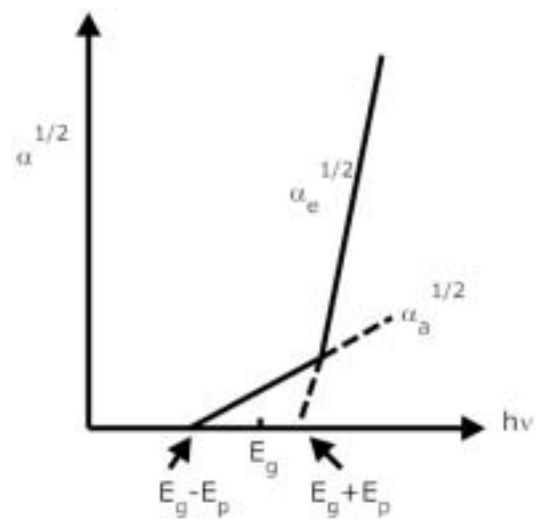

Figure 9. Absorption spectrum of an indirect semiconductor.

2.3.4 Impurity Effects on Indirect Band Transition

When a donor level is present in the semiconducting material, as shown in Figure 10, multiple absorption peaks will be present in the absorbance spectrum. There is now a level present in the bandgap that resides at an energy level E_i below the conduction band and this level allows for additional transitions to occur in the bandgap other than just E_c-E_v.

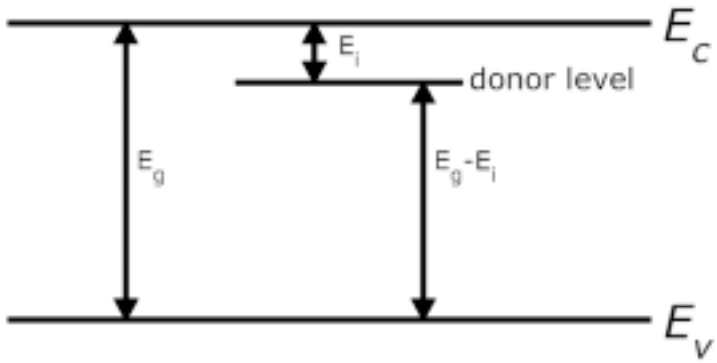

Figure 10. Bandgap with donor level.

The donor electrons will be excited from E_i to the conduction band when the incoming photon energy is greater than E_i, emptying the donor band of electrons. Since E_i is small when the impurity acts as a donor, the ionization energy is low and much smaller than the bandgap energy. Valence electrons can also be excited to the donor band when $h\nu > (E_c-E_i) - E_v$. This impurity transition energy will be close to the bandgap transition energy since E_i is small.

An impurity level in the bandgap will be noticeable in the absorbance spectrum if the quantity of impurities is large. The donor band impurities will occur as a small peak at an energy amount E_i below the bandgap absorption. This peak will occur close to the bandgap absorption peak and will appear as a shoulder in the bandgap absorption peak.

The absorption coefficient of the donor level will be proportional to the number of allowed states in the donor level. Once the incident photon energy becomes greater than E_g-E_i, electrons will begin to transition from the valence band to the donor level. Since the DOS of the valence band is greater than the DOS of the donor level, the donor level will be the limiting factor in how much absorption occurs when $h\upsilon = E_g-E_i$. The higher the DOS of the donor level, the higher the absorption coefficient will be. At high donor

concentrations and when there are sufficient phonons available to excite the donor electrons into the conduction band, the absorption coefficient for $h\nu \sim E_g$ is reduced because the DOS at the bottom of the conduction band are filled by these donor electrons so there are no available levels for the valence electrons.

A deep level trap occurs when the donor level is far from the conduction band. When the donor level is a deep level, the donor peak will be further from the bandgap absorption peak in an absorbance spectrum and therefore more distinct. However, band tailing will still convolve the absorption peaks.

These effects are not usually observed when the impurities are acceptors as the acceptor levels are generally much deeper than that of the donors and, thus, are harder to populate and depopulate thermally. Also, the DOS of the valence bands are much larger than the DOS of the conduction band due to the usually larger effective mass of the hole, m_h*. So, it is more difficult to perturb the shape of the valence band in comparison to the conduction band. In $CeO_{2-\gamma}$, there are oxygen vacancies that act as point defects within the ceria. These point defects form trap states 3 eV above the valence band in the CeO_2 bandgap. When the oxygen atoms vacate the crystal, the adjacent cerium ion is reduced from Ce(IV) to Ce(III). The CeO_2, containing Ce(IV) ions, has a bandgap of 4 eV[2].

2.4 Light Scattering

Light scattering is the process where photons, incident on some molecule or macromolecule, is scattered. The two types of elastic light scattering that occur are Rayleigh scattering and Mie scattering. The size of the scattering particle is defined as the ratio of its size and the wavelength of the incident photon written as

$$x = \frac{2\pi r}{\lambda}. \qquad \text{Eq. 21}$$

When x < 0.1, Rayleigh scattering dominates. When x > 1, Mie scattering dominates.

Mie scattering does not have strong wavelength dependence and produces a constant, flat background. Because of this constancy, it is not a significant factor in absorbance spectra deconvolution; it can simply be subtracted off. Rayleigh scattering is a significant factor in absorbance spectra because it is wavelength dependent. The intensity of scattering by a single particle from a beam of unpolarized light is

$$I = I_o \frac{1+\cos^2(\theta)}{2R^2}\left(\frac{2\pi}{\lambda}\right)^4\left(\frac{n^2-1}{n^2+1}\right)^2\left(\frac{d}{2}\right)^6, \qquad \text{Eq. 22}$$

where I_o is the intensity of the unpolarized incident light with wavelength λ. R is the distance from the particle to the detector, θ is the scattering angle, d is the diameter of the particle and n is the refractive index of the particle. In the spectrophotometry system, R, θ, and I_o are held constant. Integrating over the sphere surrounding the particle gives the Rayleigh scattering cross-section:

$$\sigma_s = \frac{2\pi^5}{3}\frac{d^6}{\lambda^4}\left(\frac{n^2-1}{n^2+1}\right)^2. \qquad \text{Eq. 23}$$

The Rayleigh scattering coefficient is the number of particles per unit volume N times the cross-section. The strong dependence on the wavelength means that more light will be scattered at lower wavelengths than higher wavelengths.

2.5 Cellular Longevity

2.5.1 Free Radical Species in Cells

The free radical theory of aging is currently the most popularly accepted explanation on how aging occurs at the molecular level due to the fact that it has significant experimental support[19-21]. The theory states that oxidative stress caused by free radicals damages cells. Over time the damage accumulates and this buildup of damage is aging at the molecular level. Oxidative stress has also been identified as a component in numerous diseases, including atherosclerosis, Arthritis and neurodegenerative disorders such as Parkinson's and Alzheimer's[22,23].

Free radicals are atomic or molecular species that are electron deficient. This deficiency causes the free radicals to be very reactive and therefore they are likely to take part in chemical reactions. In biochemistry, the free radicals are often referred to as reactive oxide species (ROS) due to the fact that the most biologically significant free radicals are oxygen-centered. However not all ROS are free radicals and not all free radicals are ROS. Examples of ROS encountered within the cell include lipid hydroperoxides, superoxide (O_2^-), the hydroxyl radical (OH•), nitric oxide (NO) and peroxynitrite ($ONOO^-$) among others[10].

ROS are formed regularly inside cells and play an important role in a number of biological processes required for normal operation. One example is the use of nitric oxide for intracellular signal transduction. When excess ROS production occurs, the cells have mechanisms capable of counteracting damage, such as superoxide dismutase, catalase and endogenous reductants, such as vitamins E and C, carotenes, melatonin and

others. When the production of ROS is too much for the innate mechanisms to counteract, the ROS induce oxidative stress within the cell.

2.5.2 Free Radical Scavengers

The treatment of oxidative stress within the cell is made difficult by the fact that as an extremely reactive species, free radicals tend not to diffuse far within the cell before taking part in a potentially damaging reaction. Another difficulty in preventing oxidative stress is that antioxidants typically have one site for free radical neutralization. This limits the effectiveness of the antioxidants since areas of oxidative stress can sustain high amounts of free radicals production.

One alternative to antioxidants that has recently been shown to be effective in protecting cells from oxidative stress is ceria nanoparticles[8,9]. Adding a dose of ceria nanoparticles to the intracellular environment of a mixed brain cell culture has been shown to increase the lifespan by up to six times. In studies where hydrogen peroxide was used to induce oxidative stress, cell death was decreased by over 60% with a 10nM dose. Ceria nanoparticles have also been shown to offer significantly greater protection than other free radical scavengers, such as vitamin E and melatonin, when aggravated by an ultraviolet light source[10].

The likely mechanism for free radical scavenging in ceria nanoparticles is the oxidation of the ceria from a Ce(III) state to a Ce(IV) state[8]. As a free radical is neutralized, a cerium ion is oxidized from the Ce(III) to the Ce(IV) state. Each exposed Ce(III) ion would act as a free radical neutralizing site and therefore a ten to twenty nanometer nanoparticle would have many more free radical neutralization sites than the other free radical scavengers. If reasonably efficient transfer of electrons from the

surface Ce(IV) to Ce(III) atoms on the interior of the ceria nanoparticle is permissible, then the number of neutralization sties can be considered to be even greater. Ceria nanoparticles have also shown the ability to auto-regenerate over time[24]. They are able to return to their original concentration of Ce(III) states after being oxidized to Ce(IV), allowing them to continuously act as free radical scavengers.

Chapter 3 Procedure

3.1 Spectrophotometry

All absorption measurements were made on a Shimadzu UV-3101PC spectrophotometer. The plots that are generated from the data collected using the Shimadzu spectrophotometer have wavelength on the x-axis and absorbance on the y-axis. Absorbance is given by the equation:

$$a = \log_{10}(I_o)\Big|_{reference} - \log_{10}(I)\Big|_{sample} \qquad \text{Eq. 24}$$

I_o is the intensity of light passing through the reference cell and I is the intensity of light passing through the sample cell. By rewriting this equation, the Beer-Lambert law is obtained:

$$I = I_o 10^{-a} \qquad \text{Eq. 25}$$

where

$$a = \alpha l c\,. \qquad \text{Eq. 26}$$

The length of the methacrylate cuvette, l, is 1 cm and absorption at wavelengths above 260 nm is negligible. α is the absorption coefficient, which is a function of wavelength and is a property of the material used. As can be seen from equations 25 and 26

absorbance is higher for a higher concentration, *c,* of the material through which light passes.

The absorption experiments in the spectrophotometer were run under two conditions: colloidal ceria suspended in water and colloidal ceria suspended in an aqueous solution at an adjusted pH.

For the colloidal ceria suspended in water, each sample was measured at a concentration of 62.5 μg/mL. These samples were suspended in deionized water with no additives to adjust the pH and no surfactants. 62.5 μg/mL was chosen as the ceria concentration for the absorption experiments for two reasons. First, mixing was made easier. The lowest setting on the micropipettes used is 100 μL, and the samples are stored at a concentration of 2.5 mg/mL. 100 μL of 2.5 mL/mg ceria and 4 mL of deionized water (the cuvettes are around 4.5 mL) works out to a ceria concentration of 62.5 mg/μL. The second and more important reason this concentration was used was that the peak absorbance for the samples was usually around a value of 2 at a wavelength of 300 nm. If the absorbance is too low (<1) the absorption spectrum will be very flat and will be difficult to resolve the 300 nm and 400 nm absorption peaks. If the absorbance is too high (>4), only a small amount of photons are incident on the detector, 0.01% of I_o when a=4. In this case, accuracy of the measurement becomes an issue as the optical signal generated at the detector is not significantly higher than its dark current.

When the hydrogen peroxide, purchased from J.T. Baker, was added to the ceria solutions, 10 μL of 0.1M was used. Such a small amount of relatively strong hydrogen peroxide is used to avoid significantly altering the concentration of the sample, which would affect the absorbance spectrum. All of the absorption measurements for colloidal

ceria solutions suspended in pure deionized water, with and without hydrogen peroxide, were measured in the very slow setting. This allows for maximum resolution and minimal noise effects.

For the colloidal ceria suspended in a pH adjusted solution, the pH was adjusted using 0.1 M sodium hydroxide and 0.1 M nitric acid, purchased from Fisher Scientific and J.T. Baker respectively. Although nitric acid eats away at the plastic beakers that most of the ceria experiments are run in, its use is necessary for pH adjustment because the chlorine ions from hydrochloric acid adsorb to the ceria, thus changing the surface properties of the nanoparticle. The pH of the solutions used ranged from 3.5 to 8.5 with one unit intervals in between. The molarity of the aqueous, pH adjusted solutions prior to the introduction of the ceria nanoparticles was on the order of 400 μM.

The pH of the ceria solutions was adjusted by adding 100 μL of 2.5 mg/mL ceria to an empty cuvette, then injecting 4 mL of the 400 μM aqueous solution into the cuvette, 1 mL at a time. The force of the ejection from the micropipette tip is enough to mix the two solutions sufficiently. An absorption measurement was then taken, approximately 10-20 seconds after all 4 mL of aqueous solution was injected into the cuvette. Another 4 mL of the 400 μM aqueous pH adjusted solution was used as the sample reference.

For the pH adjusted measurements, the medium measurement speed was used as a balance between time and accuracy. Three independent absorption spectra were taken for each sample at each pH value, then averaged together to reduce variation.

All absorption measurements were run from 260 nm to 760 nm. 260 nm is the shortest wavelength that can be used before the methacrylate cuvettes start to absorb heavily. Quartz cuvettes could have been used to perform measurements in the 200 nm

(the machine's lower bound) to 260 nm range, however nothing of interest would have been found, so methacrylate cuvettes were deemed acceptable and used exclusively. 550 nm was chosen as the upper bound because nothing of interest was noted during our initial experiments at longer wavelengths. The scattering profile of the sample can be observed when absorption is run to higher wavelengths,

3.2 Fluorometry

The fluorescence experiments were performed on a dual monochromator Jobin-Yvon spectrometer. The spectrometer is a machine that passes light through a sample and measures the fluorescence the sample emits. The light source used was a 250W tungsten halogen lamp, run at 10A, 20Vdc. The light first passes through a 250 μm slit to narrow the beam and then sent through an excitation monochromator, with a ruled diffraction grating (600 lines/mm) blazed at 350 nm. It then passes through another 250 μm slit to narrow the light spectrum incident on the sample. The input to the fluorescence monochromator had no slit and is set at a 90° angle to the sample, minimizing scattered light from entering the monochromator. The diffraction grating used in the fluorescence monochromator was a ruled grating, (600 lines/mm) blazed at 750 nm. A 500 μm slit was placed on the output of the fluorescence monochromator. The same cuvettes were used in fluorometry as in spectrophotometry. The optical signals were detected using a photomultiplier tube biased at 950V.

All experiments that were compared relative to each other were performed immediately following one another in order to prevent anomalies in the data due to variations in the current running through the tungsten lamp or to a different wavelength calibration associated with the position of the diffraction grating.

All fluorescence experiments were run with the ceria particles suspended in deionized water. When the pH of the colloidal solution was adjusted away from that of deionized water (~ pH=5.5), the particles inevitably fell out of solution faster than when they were suspended in deionized water. Since the fluorometry measurements need a very accurate concentration of the fluorophore (in this case, the ceria nanoparticles) to compare the fluorescence intensity of one sample against the fluorescence of another, any precipitation would skew the results in a random direction. Even at the low molarity used in the pH adjusted solutions, 400 μM, the particles tended to fall out too quickly to make accurate comparisons. Therefore, all fluorometry experiments were done with the particles suspended in deionized water.

The excitation wavelength in the experiments where the fluorescence spectra were collected was 420 nm and the fluorescence wavelength in the experiments to collect the excitation spectra was 550 nm. The fluorescence measurements were run with the ceria solution at 0.3 mg/mL. This concentration was used because it is high enough that a significant amount of photons will be produced but low enough that the photons can exit the cuvette with minimal scattering and/or self absorption.

The spectrometer is able to measure fluorescence in two ways. The first is an excitation scan. During an excitation scan, the fluorescence monochromator is held constant at 550 nm and the excitation monochromator is scanned across a wavelength range; the range having a center at 420 nm. The second is a fluorescence scan, which is the opposite of an excitation scan. Both methods measure the same phenomena, but one gives information about the excitation spectrum while the other gives information about the fluorescence spectrum.

Once the excitation spectra were measured, the background radiation, caused by scattered light from the sample, was subtracted from the spectra and the area of the peak was taken as the amount of fluorescence given off by that sample. The area was calculated using Origin 7.5 data analysis software made by OriginLab.

3.3 X-Ray Photoelectron Spectroscopy

XPS measurements were performed using a Perkin-Elmer 5400. To prepare the samples, an aqueous solution of 20% poly-vinyl alcohol (PVA), average mw 13,000-23,000 and purchased from Aldrich Chemical Company, was prepared. A ceria solution, suspended in DI water, with a fairly high concentration, ~40 mg/mL, was then added in equal proportions to the PVA solution to form a 10% PVA solution with a high concentration of ceria, ~20 mg/mL. A large concentration of ceria is needed due to the fact that the PVA tends to dominate the XPS spectrum unless the ceria is highly concentrated. The PVA is used as a dispersant to keep the particles separate while they dry.

The PVA-ceria solution was then put on a glass microscope slide using a Pasteur pipette. Enough solution was put on the slide to fully cover it. The slides were dried in an oven at 70° Celsius for two hours at which point the samples were ready to be loaded into the Perkin-Elmer 5400 and XPS measurements were carried out.

The areas of interest are the 3d peaks of cerium. There are 10 peaks, with 6 being associated with Ce(IV) and 4 being associated with Ce(III). All data manipulation is done with the AugerScan software package, version 3.2, produced by RBD enterprises. AugerScan is also the software used to control the XPS system. The measurement forms a continuous spectrum, which must be deconvolved into 10 independent Gaussian peaks.

By adding the area of each Ce(III) peak and then dividing by the total area, the concentration of Ce(III) can be obtained. Table 1 gives the information on the ten peaks used. To deconvolve the peaks, the spectrum is first smoothed and the background is subtracted off. Then, the ten peaks are placed and manipulated to reach a cumulative distribution that comes as close to the original spectrum as possible. Each Gaussian peak has three independent parameters: a binding energy, a peak height and a full-width half-maximum value. Once all the peaks have been placed and modified to replicate the original spectrum, the area of each peak can be calculated and a percentage of Ce(III) in the sample can be determined. Each peak was labeled with the same number in each sample's respective spectrum.

Table 1. Label assigned to each peak in the Ce 3d region of XPS spectrum along with associated binding energy and cerium state.

Peak Label	Binding Energy	Cerium State
1	882.3	4^+
2	898.4	4^+
3	900.8	4^+
4	883.3	3^+
5	902.2	3^+
6	916.5	4^+
7	889.1	4^+
8	907.4	4^+
9	880.3	3^+
10	895.9	3^+

A mean squared error (MSE) value is calculated in the software for each plot. The MSE is a common technique to quantify how close an estimator comes to matching the true value of the quantity being measured. MSE means nothing on its own but can be used to compare multiple fits against each other. The baseline subtraction used during the peak deconvolution is an approximation and leaves some residual background noise.

This noise tends to show up in the spectra between peaks 6 and 8 and between peaks 7 and 10. These remnants are ignored when the peaks are placed, but tend to inflate the MSE value. It was thus attempted to get the MSE values as low as possible, and all clustered closely, while ignoring the background remnants.

3.4 Dynamic Light Scattering

DLS was used to obtain the intensity-weighted particle hydrodynamic diameter in aqueous solution. A Malvern Zetasizer NanoZS compact scattering spectrometer (Malvern Instruments Ltd, Malvern, UK) at a wavelength of 633 nm with a 4.0 mW He-Ne laser was used at a scattering angle of 173°.

3.5 Transmission Electron Microscopy

TEM was performed on each sample in order to gain visual information about the particles. The TEM used was a Philips EM420T. Samples were prepared by drying a drop of dilute colloidal ceria on a carbon-coated copper TEM grid (400 mesh).

3.6 Brunauer-Emmitt-Teller

Surface areas of the cerium oxide nanoparticles were measured by performing BET 6-point scans using a Micromeritics ASAP 2000 nitrogen adsorption instrument. The BET measurement can be used to calculate the diameter of the particles. The specific surface area of a particle is given by

$$SSA = 6/\rho D, \qquad \text{Eq. 27}$$

where ρ is the density of the material, and D is the diameter of the particle. The density of ceria is 7 g/cm^3. The particles were assumed to be spherical and nonporous. Since it

can be seen from the TEM images that the particles are not exactly spherical, the diameter as determined from BET is treated as an approximation.

3.7 X-Ray Diffraction

XRD patterns were obtained using a Scintag XDS-2000 diffractometer with a Ni-filtered Cu-K (= 0.1541 nm) radiation source. The patterns were obtained at a scan rate of 1.0 $2\theta s^{-1}$ and were scanned from 10˚ to 90˚. Crystallite diameters were obtained using the Scherrer equation:

$$d_{XRD} = \frac{K\lambda}{\beta \cos\theta}. \qquad \text{Eq. 28}$$

The constant K is estimated as 0.9, λ is the wavelength of radiation, β is the peak width at half height in radians, and θ is the angle of reflection.

3.8 Cerium Oxide Particle Samples

All third-party samples were initially suspended in deionized water and had no surfactants. There were a total of seven samples used in this project. The NM ceria nanoparticles were purchased from Nanoscale Materials, Inc. The NM sample was synthesized using a proprietary process designed to generate large specific surface areas[25]. N160, N130 and Z1 were purchased from Nanophase Technologies Corporation. The N130 and N160 samples were synthesized via a physical vapor synthesis method where metal is vaporized, exposed to a reactant, and then condensed into nanoparticles[26]. N160 may also be referred to as Z5. Z7 is a sample synthesized by a colleague of Dr. Beverly Rzigalinski of the Virginia College of Osteopathic Medicine. Z10, purchased from Advanced Powder Technologies, is slightly different

from the rest of the particles. Z10 is the only sample whose particles fall out of suspension within a matter of minutes when suspended in deionized water. This severely limits the type of experiments that can be run on Z10. Therefore, Z10 was not used for fluorometry measurements or spectrophotometry measurements that were run with adjusted pH values. The final ceria sample used was synthesized in the Virginia Tech lab by the author and is labeled LM. The seven sample names and sources are shown in Table 2.

Table 2. Label given and respective source of ceria samples.

Sample	Source of Sample
NM	Nanoscale Materials, Inc.
N130	Nanophase Technologies Corporation
N160 (Z5)	Nanophase Technologies Corporation
Z1	Nanophase Technologies Corporation
Z7	Dr. Bev Rzigalinski
Z10	Advanced Powder Technologies
LM	Synthesized by Author

3.9 Synthesis Procedure

The procedure for synthesizing ceria was developed by Y. Xu who modified a process published in Ref. 27. The procedure uses an aqueous solvent, cerium chloride as the precursor material, and ammonium hydroxide as the reducing agent. This synthesis method is similar to other methods but is unique in that cerium chloride is used as a precursor material rather than cerium nitride [5,27,28]. Cerium chloride is a better material to use in biological applications due to the fact that leftover chlorine should not harm a biological system, as it is likely to already have chlorine in its environment.

All water used was deionized and had a resistance of 18.3 MΩ. All chemicals used were analytical grade. The ceria nanoparticles were produced by introducing a

metal salt, cerium chloride (99.9%, Alfa Aesar), into an aqueous environment. The salt breaks down and produces Ce^{3+} and Cl^- ions in the water. The solution was stirred at a rapid rate, ~500 rpms, in a plastic beaker, and kept in a water bath held at 60° Celsius during the initial synthesis stage. Ammonium hydroxide (30%, Fisher Scientific) was then added and cerium oxide nanoparticles form according to the following reaction:

$$NH_3 + H_2O \rightarrow NH_4^+ + OH^- \qquad \text{Reaction 1}$$

$$CeCl_3 \rightarrow 3Cl^- + Ce^{4+} \qquad \text{Reaction 2}$$

$$Ce^{4+} + 4OH^- \rightarrow Ce(OH)_4 \qquad \text{Reaction 3}$$

$$Ce(OH)_4 \rightarrow CeO_2 + 2H_2O \qquad \text{Reaction 4}$$

For every 20 mL of solvent, 0.25 g of $CeCl_3$ and 0.8 mL ammonium hydroxide was used, where the pH of the resulting solution was approximately 10.5. After two hours, the heat was turned off and the solution was left to spin for another 22 hours at room temperature.

The 22 hour stirring stage breaks down the large nanorods, which form in the initial reaction, into smaller nanoparticles. After the stirring stage was finished, the solution was centrifuged, rinsed with DI water, and sonicated; a process that was then repeated another two times. This process is necessary to remove as much chlorine from the surface of the nanoparticles as possible while also removing unreacted cerium and ammonium hydroxide. The sonication is necessary to break up the large agglomeration that occurs during centrifugation.

When the ammonium hydroxide was added and the reaction was initiated, the solution immediately turned light purple and slowly faded to an opaque white over the course of the heating stage. The final color of the ceria was white, with a light yellowish tint that can be seen at high ceria concentrations.

Lab-made ceria solutions that were centrifuged once were the particles used in the experiments presented in this report, and are labeled LM. LM particles are only centrifuged once because after the second and third centrifuge steps, a significant amount of ceria particles are washed off and discarded. Thus if an exact concentration is needed, centrifugation can only be run once. LM has a higher salt concentration than a sample that has been fully washed, but it has a known ceria concentration. Assuming full reactivity of the reactants, the concentration after the first wash can be calculated based on the amount of cerium chloride used. Having a known concentration is critical for the spectroscopy techniques used. An assumption was made that the differences between ceria washed three times versus ceria washed once were small and unlikely to affect experimentation results. No polymers were used in the synthesis process, either to coat the particles and prevent agglomeration[29], or to selectively grow on specific crystal planes[30]. No dopants were used to alter the reactivity of the ceria[31,32].

Chapter 4 Results and discussion

4.1 Introduction

In its most common form, ceria is stable in the nonstoichiometric form $CeO_{2-\gamma}$, where $0 \leq \gamma \leq .5$. In stoichiometric CeO_2, all of the cerium is in the Ce(IV) state. In nonstoichiometric cerium dioxide, another form of cerium oxide, Ce_2O_3, is present, where the cerium is in the Ce(III) state[33]. The reduction of the CeO_2 to $CeO_{2-\gamma}$ is caused by oxygen atoms vacating the crystal lattice, causing the cerium ions adjacent to the vacancy sites to reduce from Ce(IV) to Ce(III) [34]. The oxygen vacancies that form, leaving

oxygen depleted Ce(III) ion behind, are believed to be the cause for the high reactivity in ceria[35].

Cerium oxide has a cubic fluorite structure, both in bulk and nanoparticle form[36]. The low index exposed crystal planes have been shown to have differing reactivity[37]. The {111} surface plane is the most stable, followed by the {110} and {100} planes. The formation of an oxygen vacancy occurs more easily for the {110} surfaces than in the {111} surfaces. The vacancies tend to form in the surface layer for {110} whereas for the {111} surface they tend to form in the subsurface layer[38].

Quantum confinement is not considered when analyzing ceria nanoparticles. If quantum confinement of the electrons and holes were present, then a blue-shift would occur in the absorption curves for smaller particles. In published studies, smaller particles have shown a red-shifted bandgap[2]. The reason ceria nanoparticles have an opposite effect to that observed in other semiconducting nanoparticles is not because of a quantum mechanical phenomenon, but rather that, as the particles get smaller, they have a higher ratio of Ce(III) to Ce(IV)[39-41]. This increase in Ce(III) ions within the crystal lattice causes a red shift in the absorbance of the material; attributable to the defect states associated with the Ce(III) ions and oxygen vacancies. The defect states reside 3eV above the CeO_2 valence band. The CeO_2, containing Ce(IV) ions, has a bandgap of 4eV. As the concentration of Ce(III) ions increases, the concentration of Ce(IV) ions decreases and more absorption will occur at 3eV and less at 4eV, causing a redshift in the absorption spectrum.

4.2 Particle Size

4.2.1 Sample Size Comparison

Table 3 shows the agglomeration size, as determined by DLS, the individual particle size, as determined by TEM, XRD and BET, and the specific surface area of each sample, as determined by BET. The TEM particle size is given as a range. BET and XRD were not performed on all samples.

There is two size ranges as determined by the TEM images given for the samples. This is due to the fact that the Z7 sample and the Nanophase samples possess a very wide size distribution. In reality, there is no discreet break between the large and small particles in these samples. The large and small particles are separated here because important information about the exposed surface planes can be determined by examining the large particles while the small particles are too small to view anything of value.

Table 3. The particle size as determined from TEM, diameter measured by DLS, crystallite size determined from XRD, specific surface area measured from BET and diameter calculated from specific surface area.

Sample	TEM-Small Particle Size Range(nm)	TEM-Large Particle Size Range (nm)	DLS-Diameter (nm)	XRD-Crystallite Size (nm)	BET-Specific Surface Area (m^2/g)	BET-Diameter (nm)
NM	5-7	None	245	4.2	86.0	10.0
N130	4-6	15-100	130	N/A	88.6	9.7
N160	3-10	10-150	160	37.9	24.6	34.8
Z1	3-10	10-80	160	N/A	N/A	N/A
Z7	3-10	10-150	152	N/A	N/A	N/A
Z10	4-6	None	184	N/A	N/A	N/A
LM	7-9	None	114	N/A	55.9	15.3

4.2.2 NM

The DLS size of the NM sample, 245 nm, indicates that there is a great deal of agglomeration, which was confirmed from the TEM images shown in Figure 11. There are no visible single particles in the TEM images, all the particles have agglomerated. There appears to be a narrow size distribution with the NM particles. The individual particle range as determined from TEM, 5-7 nm, matches well with the crystallite size, 4.2 nm, and the particle size as determined by BET, 10 nm.

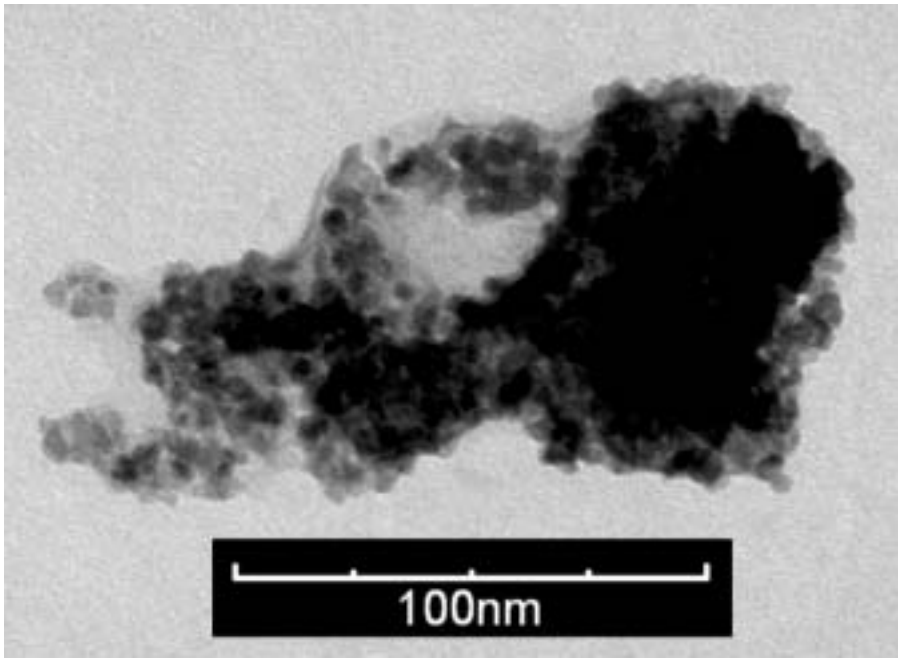

Figure 11. TEM image of NM.

4.2.3 N130

There were two types of particles present in the TEM images of the N130 sample, shown in Figure 12. There were small particles with an average diameter of 5 nm as determined from the TEM images. These form smaller agglomerates than the NM particles. Particles with eight faces forming an octahedron shape are also present. These octahedra are larger particles, ranging from 15 to 100 nm in diameter, and show little to no agglomeration. The octahedra appear to have the {111} crystal facet exposed on all eight faces. The primary particles are too small to observe which crystal facets are exposed.

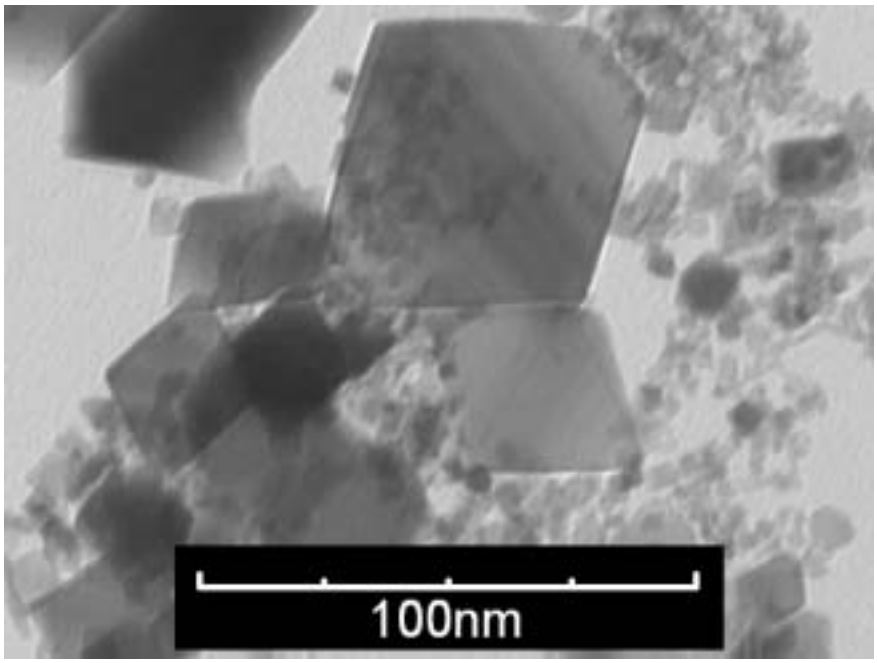

Figure 12. TEM image of N130.

4.2.4 N160

The DLS size of the N160 sample and the TEM images (Fig. 13) show that N160 is very similar to N130, except with slightly larger octahedra. The crystallite sizes of the N160, 37.9 nm as determined by XRD, and the diameter determined by BET, 34.8 nm, match up well with the particles shown in the TEM image.

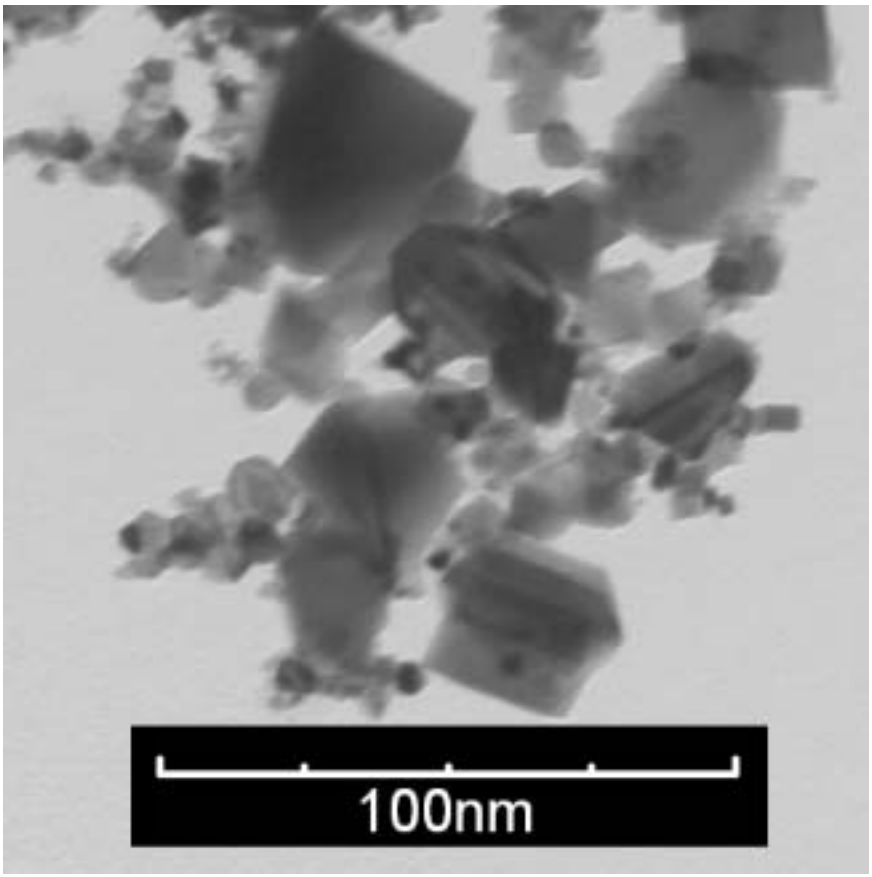

Figure 13. TEM image of N160.

4.2.5 Z1

The DLS size of the Z1 sample and the TEM images (Fig. 14) show that Z1 is also similar to N130 and N160. Z1 has the tightest size distribution of the Nanophase samples and the smallest octahedra, with the largest being 80 nm.

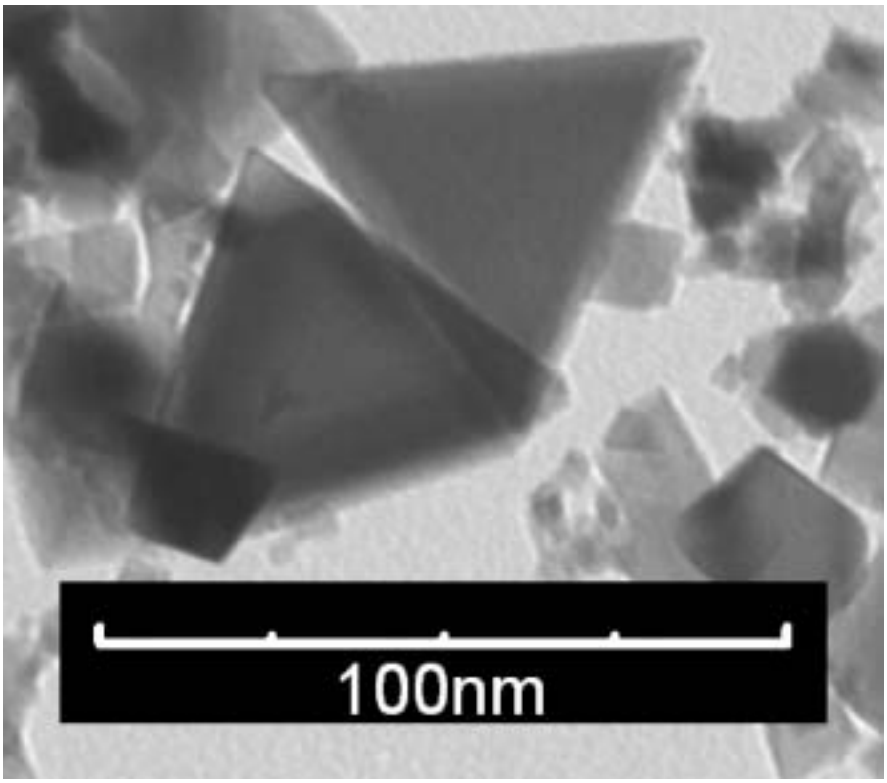

Figure 14. TEM image of Z1.

4.2.6 Z7

As shown in the TEM images of Z7 in Figure 15, Z7 is made up of octahedra and smaller particles similar to the Nanophase samples. Z7 has a very wide size distribution with particles ranging from 3 nm to 150 nm.

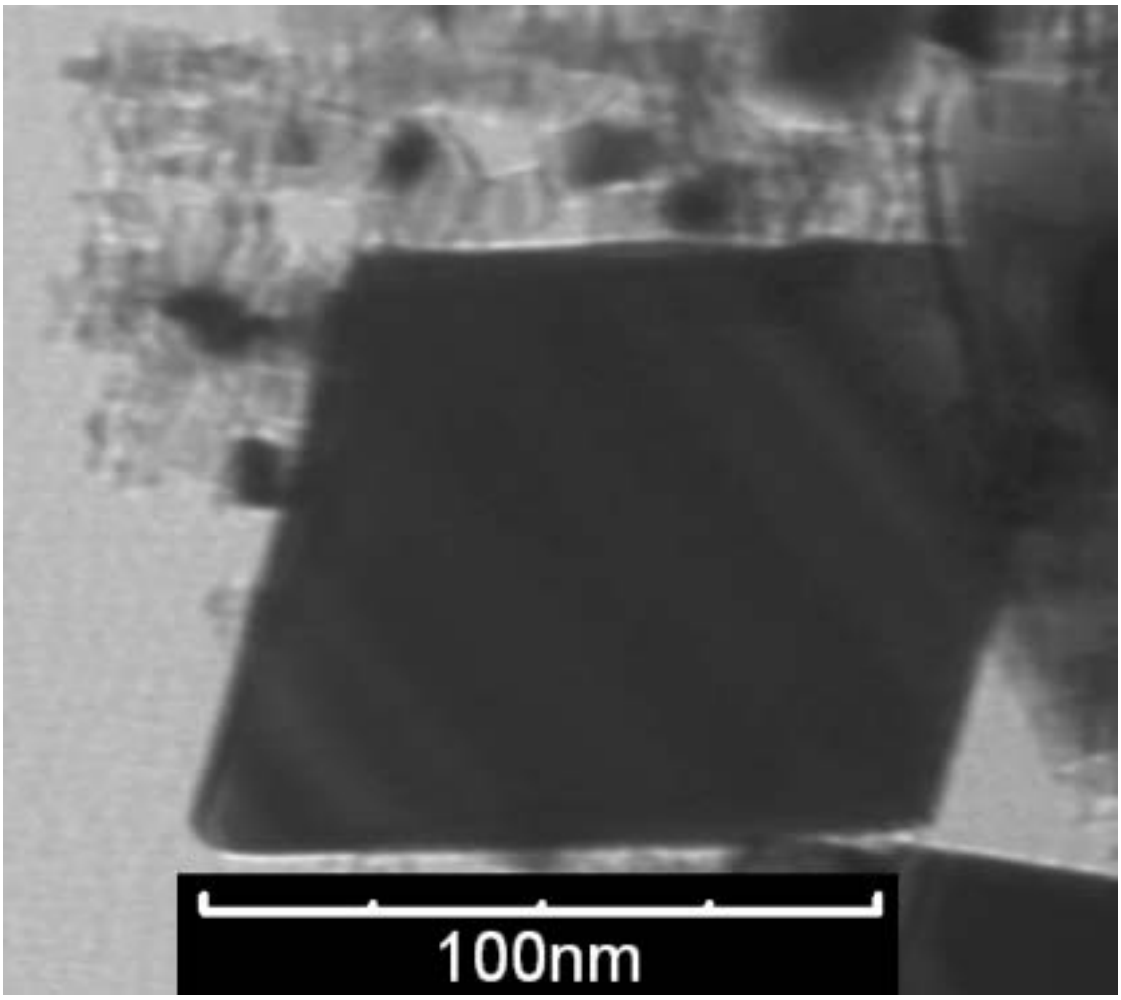

Figure 15. TEM image of Z7.

4.2.7 Z10

The TEM images show that Z10 is made up only of smaller particles, similar to NM. Figure 16 shows the TEM image of the Z10 sample, where the average diameter is 5 nm. There is a significant amount of agglomeration, as shown by the difference between the DLS size, 184 nm, and the individual particle size, 5 nm as determined by TEM.

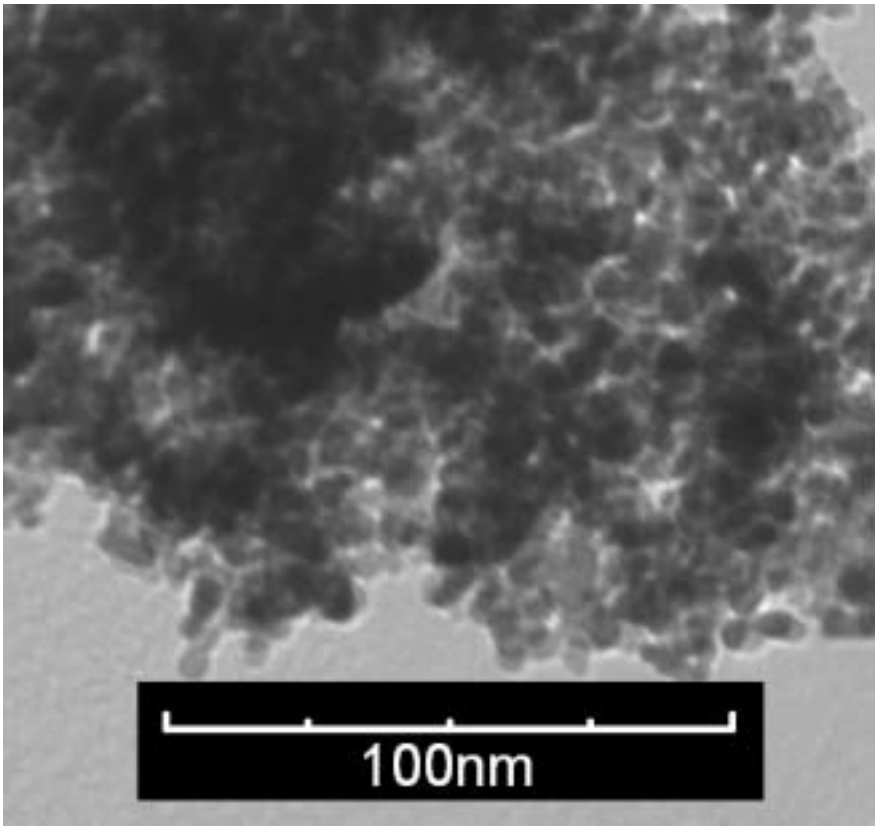

Figure 16. TEM image of Z10.

4.2.8 LM

The TEM images show that LM is made up only of smaller particles similar to Z10 and NM. The particles have an average diameter of 8 nm as determined from the TEM images shown in Figure 17. There is much less agglomeration in the LM sample than NM and Z10, as shown by the DLS size of 114 nm, but there are still no non-agglomerated particles present.

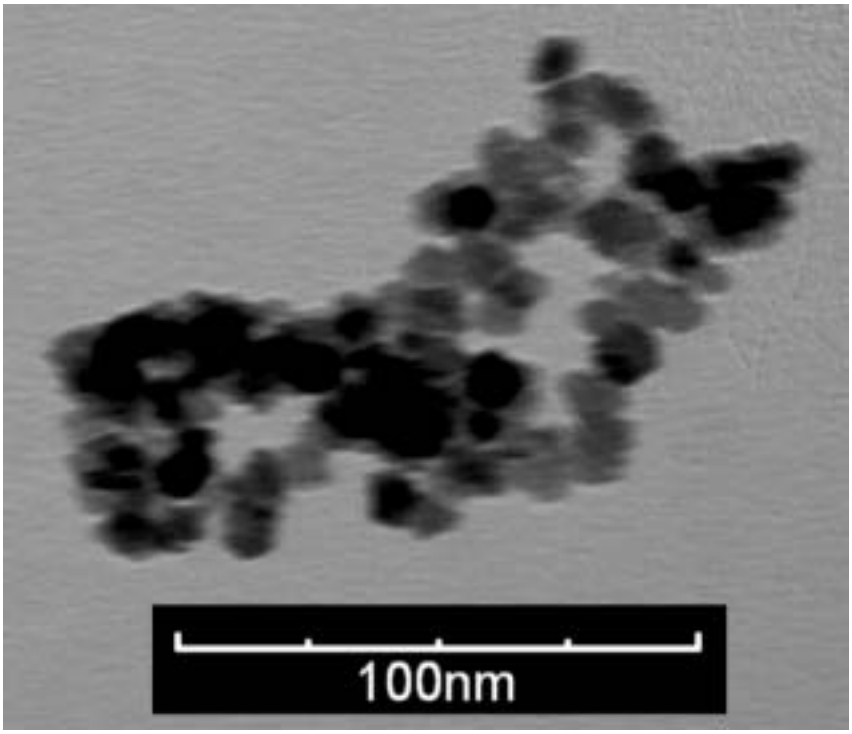

Figure 17. TEM image of LM.

4.3 Characterization

4.3.1 Spectrophotometry

The spectrophotometry results can give important insight into the band properties of cerium oxide. In a defect-free semiconducting crystal, the absorbance will be nearly zero at low energy until photon energy approaches the bandgap energy of the crystal [16], at which point the absorption should increase rapidly. When a small concentration of a second material that possesses lower band gap energy is present in the crystal or defects are present that modify the DOS, the slope of the absorption edge will lessen. In traditional optoelectronical studies, these ions are considered defects and are undesirable[16]. However in cerium oxide, the Ce(III) ions that arise near oxygen vacancies and near grain boundaries are desirable from a reactivity standpoint. Many studies have been done to synthesize particles that have a higher ratio of Ce(III)/Ce(IV) [5,41,42].

The band gap of CeO_2 is roughly 4eV[2]. This is an indirect gap of the $O2_P$ to the $Ce4_f$ molecular transition. Ce(III) ions present in the crystal lattice create a trap state 3 eV above the CeO_2 valence band and correspond to the $Ce5_d$ - $Ce4_f$ transition. A photon with 3 eV of energy will possess a wavelength of approximately 413 nm and a photon with 4 eV of energy will possess a wavelength of approximately 310 nm. To determine whether scattering would be an issue, the DLS size was put into equation 21. In the visible wavelength range and for the size of aggregated particles this study deals with, Rayleigh scattering should not be a factor and Mie scattering should dominate. Since Mie scattering is not wavelength dependent, it is easily removed from the spectra through a baseline subtraction. Figure 18 shows the spectra of all seven samples, each at 61

μg/mL, without normalization and without subtraction of the Mie scattering. Figure 19 shows the spectra of all seven samples, each at 61 μg/mL, where each curve was normalized by dividing the absorbance at each wavelength by the absorbance at the 300 nm, but no attempt was made to remove the effects of scattering. Figure 20 shows the spectra of all seven samples, each at 61 μg/mL, where scattering was removed by subtracting the magnitude of the absorbance at 760 nm, a wavelength at which no absorption by ceria occurs, from each data point in the absorption spectra. After that, each curve was again normalized by setting the magnitude of the 300 nm peak to a value of one. The absorbance of each sample at 400 nm was then compared.

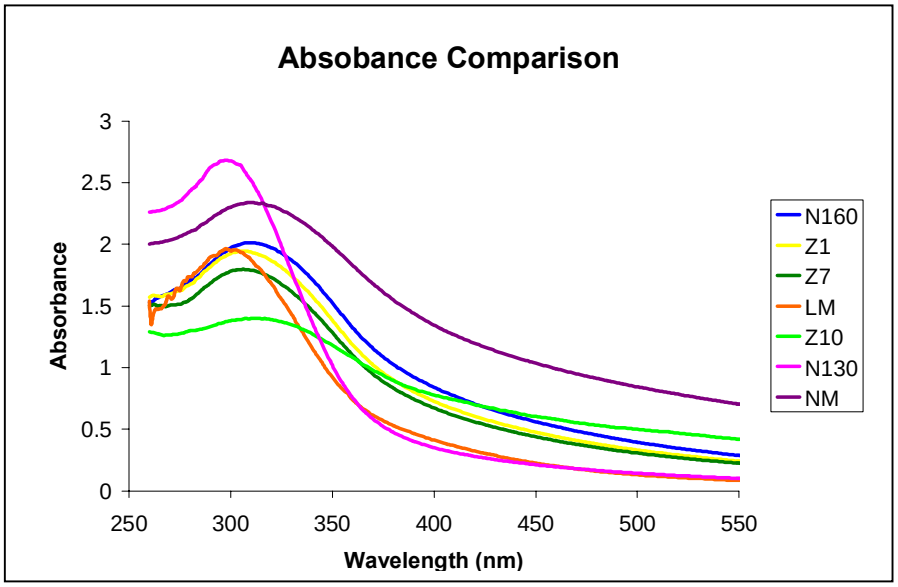

Figure 18. Absorbance spectra of all samples.

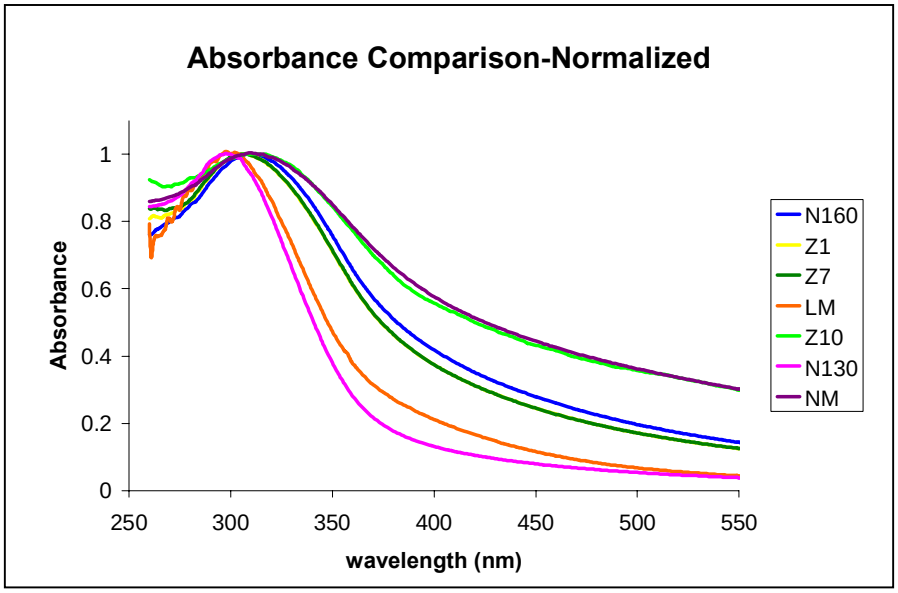

Figure 19. Absorbance spectra of all samples with peaks normalized to one.

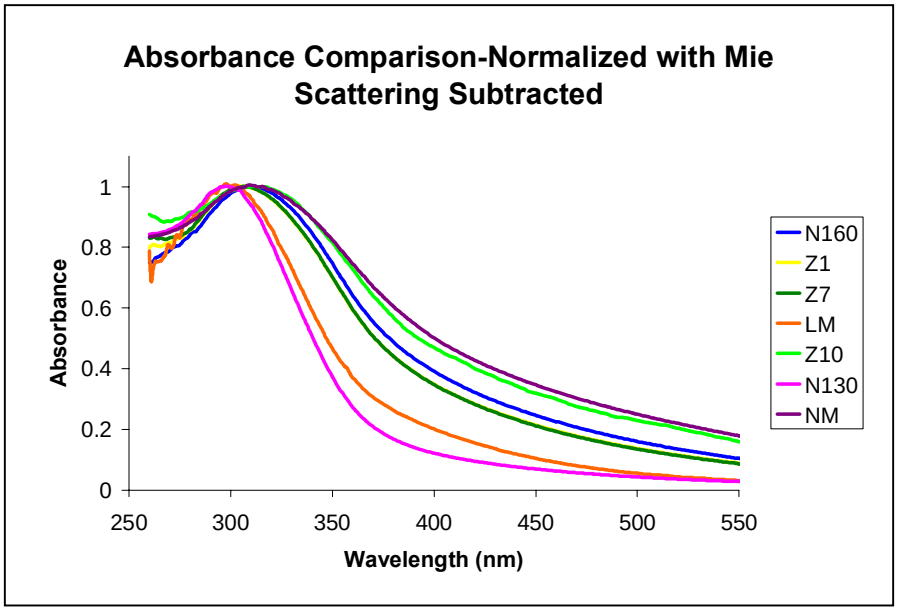

Figure 20. Absorbance spectra of all samples with Mie scattering removed and peaks normalized to one.

The 300 nm peak corresponds to the CeO_2 bandgap and can therefore be attributed to the Ce(IV) while the 400 nm peak corresponds to the defect state and therefore can be attributed to Ce(III). NM has the highest absorbance at 400 nm and N130 has the lowest value in Figure 20. The N130 absorbance falls off significantly by 380 nm and falls nearly to zero as it extends out past 450 nm. The peak of the NM absorption spectrum is at 312 nm, a slight redshift compared to N130, but the biggest difference is how the magnitude of the slope of the absorption spectrum as the wavelength increases. While the N130 absorbance falls off rapidly, the absorption curve of NM has a very gradual slope at longer wavelengths. The normalized absorbance of each sample at 400 nm is shown in the Absorbance column of Table 5.

For solutions of the same concentration, N130 absorbs greater at 300 nm and NM absorbs more at 400 nm. This is an indication that there is a smaller ratio of Ce(III)/Ce(IV) in the N130 than the NM sample. To describe the absorption spectra in terms of the optical transitions in CeO_2, the energy band diagram of ceria is shown in Figure 21, where the Ce(III) ion is identified as a defect state. As mentioned in Chapter 2, the presence of defect states, Ce(III), will cause absorption of photons with energy less than the bandgap of CeO_2 and will cause the absorption coefficient to increase more gradually than for pure CeO_2.

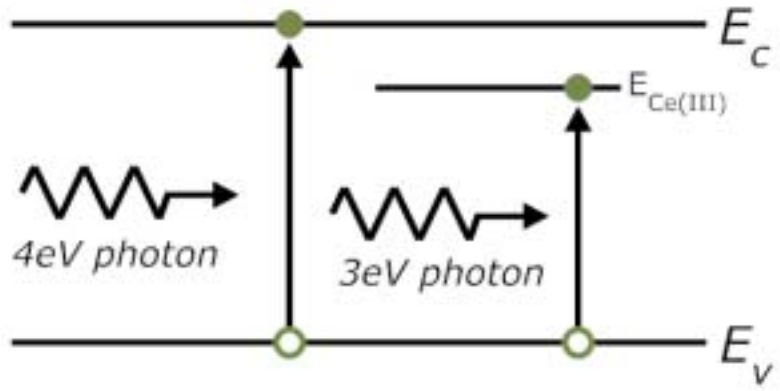

Figure 21. Bandgap of Ceria with Ce(III) trap states.

The amount of oxygen vacancies on the surface of the ceria nanoparticles is mildly dependent on pH[43]. According to the Lewis definition of acids and bases, Ce(III) is a base and Ce(IV) is an acid. Therefore, a more basic solution will create more Ce(III) ions on the surface of the nanoparticles and a more acidic solution will create more Ce(IV) ions on the surface. To show that spectrophotometry would detect the change in Ce(III) ion concentration as a function of pH, spectrophotometry was run on each sample (except Z10) with the pH of each sample adjusted to values of: 3.5, 4.5, 5.5, 6.5, 7.5 and 8.5. For each sample, six absorbance spectra, one for each of the six pH values, were plotted on the same graph. The magnitudes of the absorbance at 300 nm and 400 nm have been plotted versus pH to determine the trend that the 300 nm and the 400 nm peaks take as a function of pH. The absorbance spectra of N160 at each pH level are shown in Figure 22. The spectra at higher pH can clearly be seen to have a lower absorbance at 300 nm than the higher pH spectra. This agrees with theory and is an indicator that spectrophotometry can be a sensitive measurement for changes in the Ce(III) and Ce(IV) concentrations of a ceria sample.

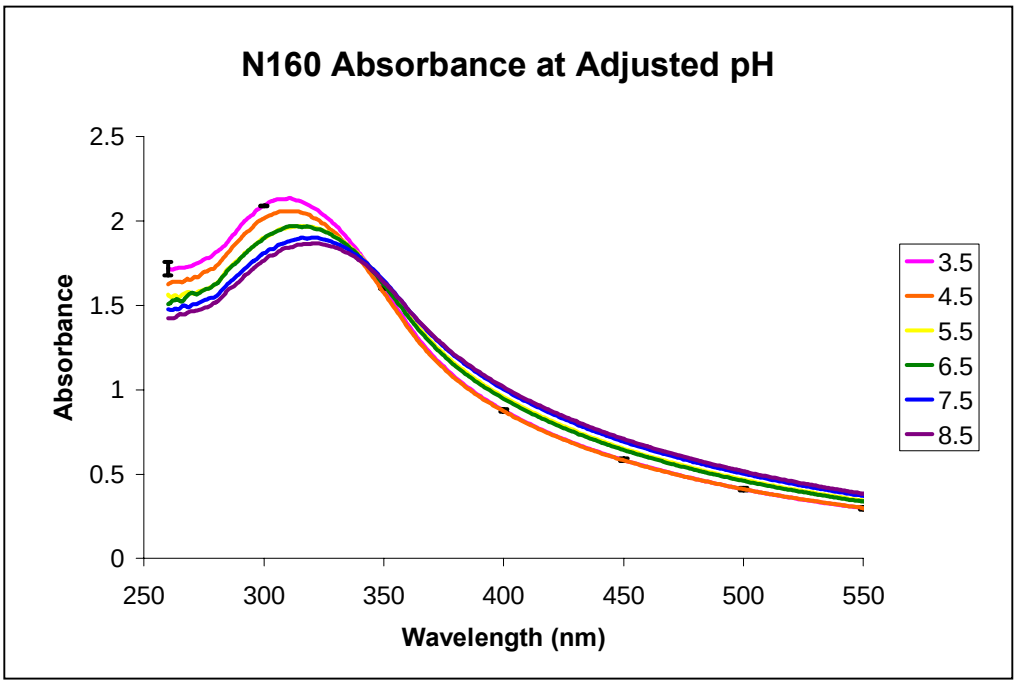

Figure 22. Absorbance spectra of N160 with adjusted pH.

Figure 23 shows the plots of the absorbance magnitude at 300 nm versus pH and the absorbance magnitude at 400 nm versus pH for the N160 sample. The fact that the absorbance rises at 400nm and falls at 300nm as pH rises indicates that the concentration of Ce(III) is rising. The slope of the absorbance magnitude at 300 nm versus pH and the slope of the absorbance magnitude at 400 nm versus pH are consistent in each sample; the absorbance of each sample falls at 300 nm and rises at 400 nm as pH rises. To show the variation between the absorbance spectra, error bars have been added to the absorbance spectrum at a pH of 3.5 for each sample. These black lines show the maximum and minimum values of the three spectra used every fifty nanometers. All of the samples absorbance spectra at different pH levels and their subsequent plots of absorbance magnitude at 300 nm and 400 nm are shown in Appendix A.

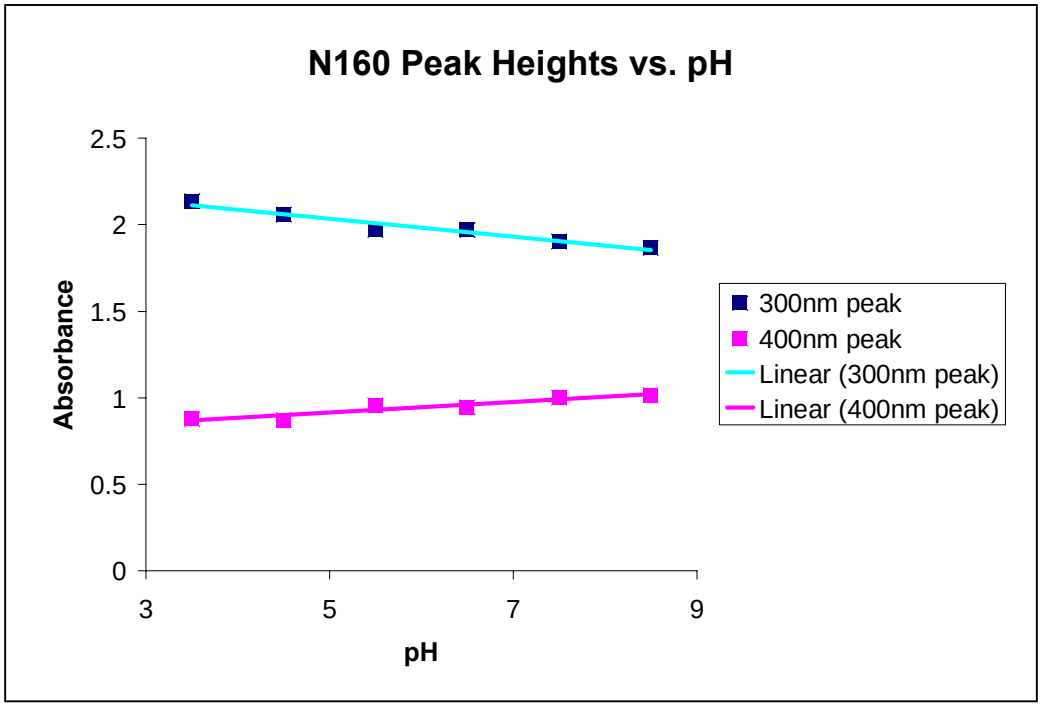

Figure 23. Values of 300 nm peak and 400 nm peak versus pH for N160.

Figure 24 shows the absorption spectrum of N160 along with the absorption spectrum after it has been oxidized. One unexplained phenomenon that occurs with each ceria sample is that the absorbance at 400 nm increases after being oxidized by hydrogen peroxide. This is the opposite of the expected result. The hydrogen peroxide should decrease the Ce(III) concentration, which absorbs at 400 nm, causing a drop in absorbance at 400 nm. But the opposite occurs and this cannot currently be explained. No useful information can be gained from the ceria absorption peak at 300 nm when hydrogen peroxide is added as the peroxide begins to absorb at 350 nm and convolutes the spectrum. The oxidized and unoxidized absorption spectra of each sample can be found in Appendix B.

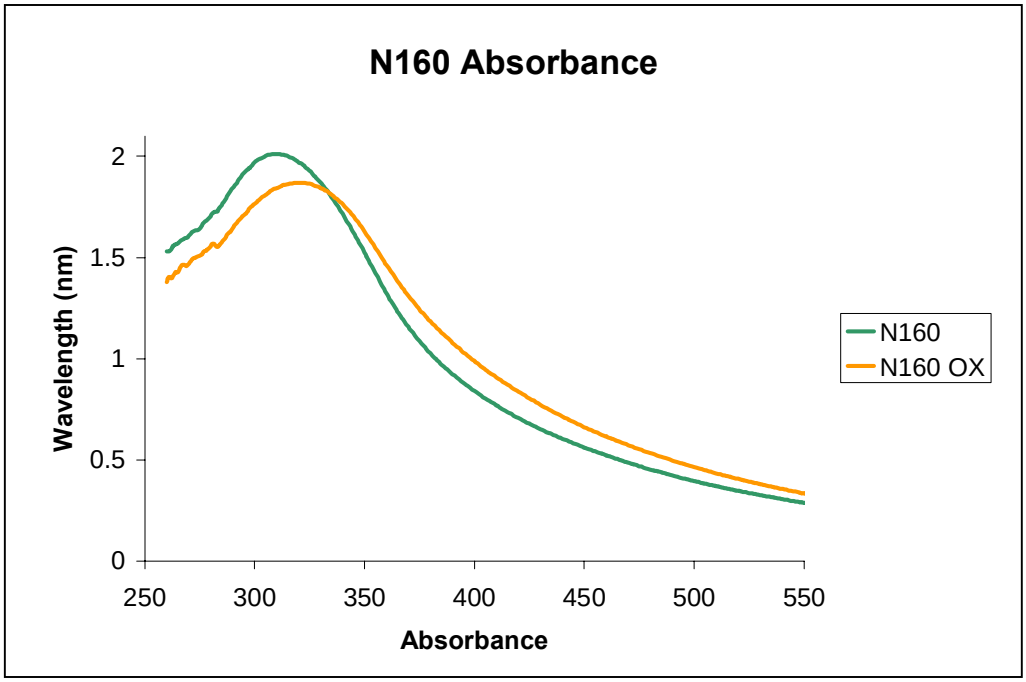

Figure 24. Absorbance spectra of N160 before and after being oxidized.

4.3.2 Fluorometry

The 4 eV bandgap of ceria is an indirect gap, therefore there will be a very small probability that radiative recombination will occur when absorption takes place[2]. Relaxation via the 5d-4f transition of the Ce(III) ions does result in photon emission though. The ceria is excited with 420 nm light, causing the valence band electrons to transition to the defect state within the bandgap. From the defect state, the electron will undergo multiple transitions in order to return to the ground state. The light emitting transition emits a photon with wavelength 550 nm; the rest are non-radiative.

According to equation one, the rate at which photons are emitted from the material via spontaneous emission is proportional to the number of excited electrons in the conduction band. When more Ce(III) states are available, more electrons are able to

become excited and therefore more photons are emitted. Higher fluorescence indicates that there is a higher concentration of Ce(III) states to provide electrons.

Figure 25 shows the fluorescence spectrum collected from each sample sans Z10 with the base of each set to zero. The minor differences in the peak wavelength of the fluorescence spectrum can be attributed to the precision of the monochromator stepper motor. It can be seen in the figure that intensity of the fluorescence spectrum from the NM sample has the highest intensity and that of N130 the lowest. Since the area is proportional to the peak height, the amount of fluorescence of each sample can be roughly determined from the figure. After analyzing the area of each sample through mathematical software, it is determined that NM has the highest concentration of Ce(III) and N130 has the lowest concentration. The area of each sample has been is shown in the Fluorescence column in Table 5. The amount of fluorescence appears to be proportional to the absorption at 400 nm for the samples. The results of spectrophotometry and fluorometry match each other closely.

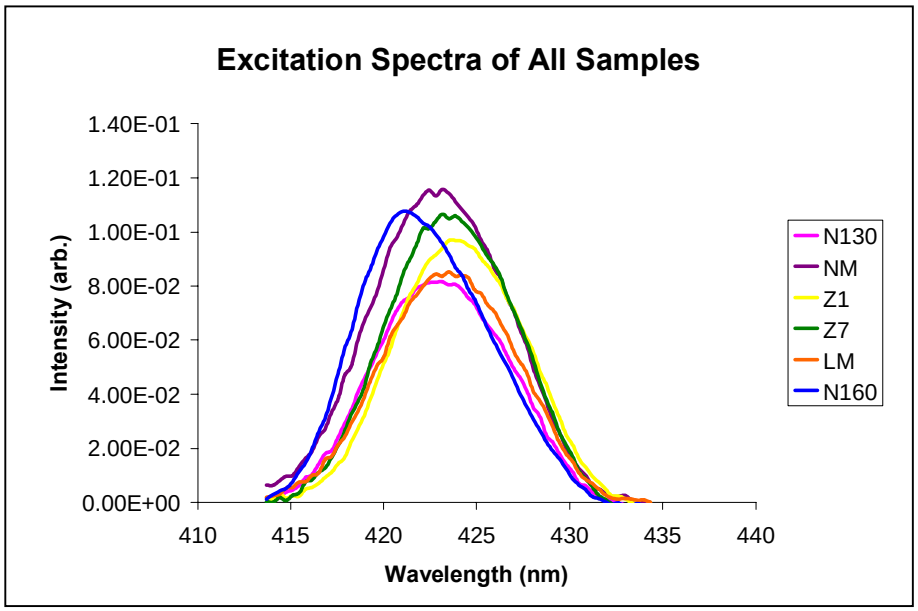

Figure 25. Fluorescence of each sample after baseline subtraction.

To show that the Ce(III) ions are responsible for the fluorescence, hydrogen peroxide was added to the sample. 10 µL of 0.1M hydrogen peroxide was used to oxidize the ceria to show that the fluorescence came from the Ce(III) ions and not the Ce(IV) ions. The hydrogen peroxide oxidizes the Ce(III) to Ce(IV) and the fluorescence can be attributed to the Ce(III) cerium ions since a drop in the fluorescence was detected. Figure 26 shows the fluorescence and excitation spectra along with the oxidized spectra for the NM sample. The fluorescence and excitation spectra of each sample can be seen in Appendix C.

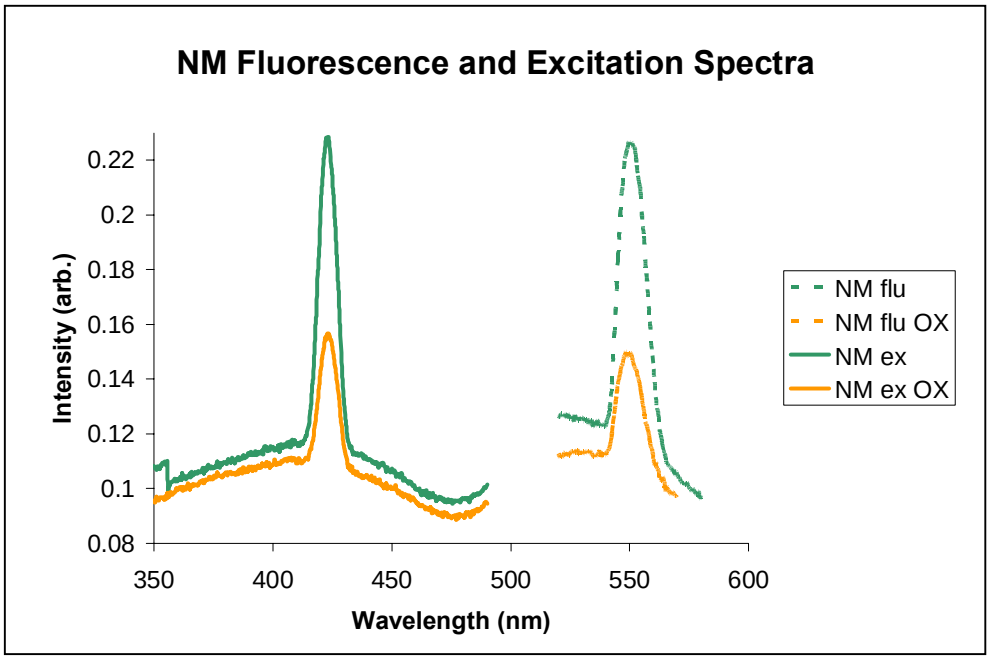

Figure 26. Fluorescence and excitation scan of NM before and after oxidation.

4.3.3 X-Ray Photoelectron Spectroscopy

XPS is a well defined characterization technique frequently used to determine the chemical states of ions in materials. In this study, XPS is used to determine the concentration of Ce(III) in a sample to a high degree of accuracy. The XPS spectrum of

NM, with Gaussian curves, is shown in Figure 27. The measured curve is a black solid line. The Gaussian curves added are dotted lines, with green used for Ce(III) peaks and blue used for Ce(IV) peaks. The curve generated by the Gaussian peaks is a solid yellow line. Table 4 gives the values used for each Gaussian peak. Peaks 4, 5, 9 and 10 are associated with Ce(III) and the rest are associated with Ce(IV).

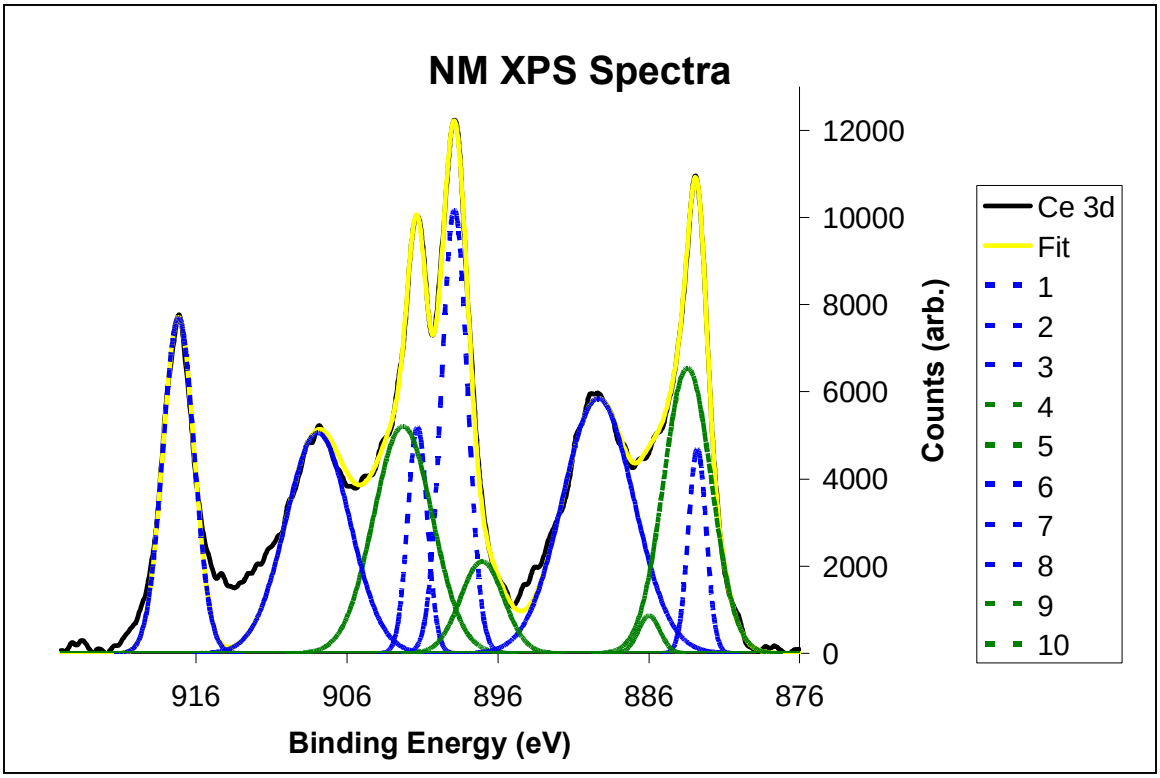

Figure 27. Measured and fitted XPS spectra of NM along with ten Gaussian peaks.

Table 4. Gaussian peak parameters for XPS spectrum of NM. NM had an EMS value of 10.72.

#	Area	Area%	Position	Intensity	FWHM
1	4657	3.90%	882.78	3125	1.4
2	14668	12.30%	898.87	6788	2.03
3	5605	4.70%	901.32	3464	1.52
4	1026	0.90%	885.97	577	1.67
5	16863	14.10%	902.28	3474	4.56
6	13306	11.20%	917.15	5144	2.43
7	23076	19.30%	889.35	3899	5.56
8	17773	14.90%	907.92	3373	4.95
9	17289	14.50%	883.43	4366	3.72
10	5017	4.20%	897.04	1407	3.35

According to the spectrophotometry and fluorometry measurements, NM should have the highest amount of Ce(III) present. The amount of Ce(III) as determined by XPS is 33.7% and the EMS value is 10.72. The Ce(III) concentration corresponds to a γ value of 0.169. The XPS spectrum of N130, which should have the lowest amount of Ce(III) present according to the spectrophotometry and fluorometry measurements, is shown in Figure 57. The amount of Ce(III) in N130 as determined by XPS is 27.9% with an EMS value of 13.8. This value corresponds to a γ value of 0.140. The Ce(III) concentration as determined by XPS for all samples can be seen in Table 5. The Ce(III) concentrations match up very well with the optical spectroscopy results, with Z10 having the highest Ce(III) concentration, followed by NM having the second highest Ce(III) concentration and N130 with the least.

To determine the amount of variation from run to run, the XPS spectrum of N160 was measured three times. The Ce(III) concentrations found were 30.6%, 31.4% and 31.5% with EMS values of 6.5, 10.12 and 10.59 respectively. The second and third measurements, which have EMS values that differ by less than 0.5, correspond to Ce(III) concentrations that differ by a tenth of a percent. This tiny amount of variation between runs indicates that the run to run variation of the XPS system is negligible. The N160 spectra and all other XPS spectra can be found in Appendix D.

4.3.4 X-Ray Diffraction

XRD was performed to find the probability of a preferred orientation for the surface planes in the ceria nanoparticles. The ratio $A_{(111)}/A_{(200)}$ gives the probability that one plane will occur predominantly in the sample. Since the {111} plane has a lower

propensity for oxygen vacancies than the {200} plane [38], the samples with a higher concentration of Ce(III) should have a higher $A_{(111)}/A_{(200)}$ ratio[42].

The $A_{(111)}/A_{(200)}$ of N160 is 11 and 5 for NM. This would indicate that N160 has a higher amount of {111} surface planes exposed than the NM sample. It was shown in section 4.2 that the Nanophase samples had clearly visible {111} surface planes exposed in the larger ceria particles. As the oxygen vacancies are more likely to form in the {200} planes than in the {111} planes, this may explain the higher concentration of Ce(III) found in NM than in N160. With a higher propensity for oxygen vacancies in the exposed surface, we would expect that NM would be the most reactive particle. This is confirmed in Ref. 15 and the reactivity constants are shown in Table 5. Figure 28 shows the XRD spectra of NM and N160.

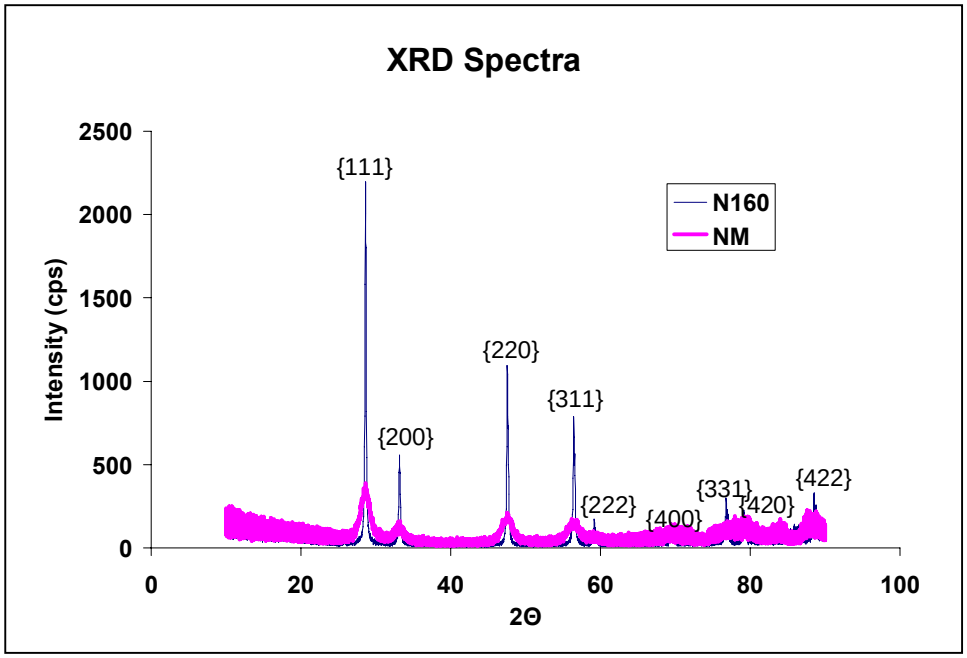

Figure 28. XRD spectra of NM and N160.

4.3.5 Sample Comparison

Table 5 gives the absorbance values at 300 nm and 400 nm for each sample; the fluorescence area under the excitation peak for each sample; the concentration of Ce(III) ions in each sample as determined by XPS and its corresponding γ value in $CeO_{2-\gamma}$; the $A_{(111)}/A_{(200)}$ ratio for each sample and the reactivity constant as determined by Ref. 15. The N160 XPS value is the average of the three measurements taken.

Of the samples where fluorescence and absorption experiments were performed, NM had the highest absorbance at 400 nm, the highest fluorescence and the highest concentration of Ce(III) ions as determined by XPS. N130 had the lowest absorption at 400 nm, the lowest fluorescence and the lowest Ce(III) concentration as determined by XPS. The 400 nm absorbance column and the fluorescence area column seem to correspond very well with each other, with each column following the same descending order. The only aberration of the XPS column is that Z10 had a lower absorbance than NM and Z7 had a higher fluorescence than Z1.

Table 5. Final comparison of all data obtained from spectrophotometry, fluorometry, XPS, XRD and reaction kinetics.

Sample	Abs. at 300 nm	Abs. at 400 nm	Flu. Area	XPS-Ce(III) Concentration	γ	$A_{(111)}/A_{(200)}$ Ratio	Reactivity Constant
NM	1	0.576	1.076	33.7	0.169	5	0.0374
Z10	1	0.557	N/A	34.5	0.173	N/A	N/A
N160	1	0.418	0.935	31.2	0.156	11	0.012
Z7	1	0.375	0.9156	29.6	0.148	N/A	N/A
Z1	1	0.375	0.846	31.0	0.160	N/A	N/A
LM	1	0.211	0.774	28.2	0.141	N/A	0.0459
N130	1	0.131	0.743	27.9	0.140	N/A	0.0137

Chapter 5 Conclusion

Seven cerium oxide samples were compared against each other using spectrophotometry, fluorometry and XPS data to observe differences in Ce(III) and Ce(IV) concentrations. The amount of Ce(III) in each sample is important because it increases the reactivity of the particles, which may have a beneficial effect on the lifetime of cells by reducing the concentration of ROS.

Fluorescence of the all the samples at the same concentration was measured and NM was found to have the highest fluorescence while N130 had the least. Confirmation that the fluorescence originated from the Ce(III) ions was shown by oxidizing the Ce(III) to Ce(IV) in both samples and observing a drop in the fluorescence. Spectrophotometry data was taken of the samples and the results were examined closely to determine the optical properties of cerium oxide as a function of Ce(III) and Ce(IV) concentrations. The Ce(IV) was the dominant ion in all the samples. CeO_2, where the cerium is Ce(IV), has a band gap of 4eV. Point defects, caused by oxygen vacancies and where the Ce ion has been reduced from Ce(IV) to Ce(III), exist 3eV above the valence band in the CeO_2 bandgap. When the absorption spectra of the samples were measured at the same concentrations and that data was processed such that the effects of Mie scattering were removed and the peaks normalized, the samples that absorbed much more heavily at 400 nm were found to have a higher concentration of Ce(III) ions. NM absorbed the most at 400 nm, indicating the highest concentration of Ce(III). N130 absorbed the least, indicating the least amount of Ce(III).

The last spectroscopy method employed to determine the Ce(III) concentration was XPS. In this study, it was determined by XPS that Z10 had the most Ce(III), NM

had the second most Ce(III) and N130 had the least Ce(III). The observance of Ce(III) and Ce(IV) in the XPS spectra therefore strongly reinforces the validity of the absorption and fluorescence results.

Finally, XRD spectra were taken in order to determine the probability of a favored crystal surface in the particles. The XRD spectra can be used to explain why a particular sample had a higher concentration of Ce(III) than another sample due to the {111} crystal planes having the lowest propensity for oxygen vacancies. The NM had a lower $A_{(111)}/A_{(200)}$ ratio than N130 and N160 and this may explain why it has a higher concentration of Ce(III) than them.

Of the samples where the optical spectroscopy was performed, it was determined that NM had the highest Ce(III) concentration while N130 had the lowest concentration. It was also shown that Z10 had the highest amount of Ce(III) out of all the samples. The Ce(III) concentrations determined through absorption, fluorescence and XPS data matched up well, with only the occasional aberration.

Chapter 6 Future Work

6.1 Spectroscopy

The spectroscopy methods discussed so far have all been defined on particles acquired from third-party vendors, along with one sample synthesized in the lab. This limits the degree to which the characterization methods themselves could be characterized. Given a wider range of particles, particularly those that contain significantly higher concentrations of Ce(III), the spectroscopy methods could be further refined. Although this method works well, it is possible that a better understanding of the

composition of the ceria nanoparticles could be obtained from the analysis of the spectrum.

6.2 Scattering

The biggest source of ambiguity in these characterization methods is the scattering in the absorption spectrum. There are a few experiments that could be run to further characterize the scattering in the system. Absorption spectra of agglomerated versus non-agglomerated ceria particles could be used to determine the difference in the scattering profile due to Mie and Rayleigh scattering. With more lab time and with better defined particles, the assumptions that were made could be verified. Once it was known exactly how much Rayleigh and exactly how much Mie scattering was occurring, it would be much easier to deconvolve the absorption peaks from the scattering profile.

6.3 Synthesis

The initial thrust of this research project was to further refine the ceria synthesis project started by Yang Xu; this changed when it was realized that there was no quick screening method for the Ce(III) concentration of a sample. The only method available to was to run XPS, which would be too costly and inefficient to run on every batch of particles synthesized. This started the search for a quick screening method to determine the concentration of Ce(III) ions in the samples and ended with the spectroscopy methods outlined in this report; however successful the study of spectroscopy methods have been, the synthesis project was left completely untouched.

There are a number of experiments that could be run to further refine the synthesis process of cerium oxide. By changing synthesis factors and examining the effects caused

by each change, a greater control of the material properties of the particles can be achieved.. The first major synthesis factor that could be changed is the temperature at which the particles are synthesized. A study on the effect that temperature had on the shape of the nanoparticles have been previously published[42]; however, no optical measurements were performed on these nanoparticles nor was the Ce(III)/Ce(IV) determined. The ability to adequately replicate the results would allow us to produce particles with a wide range of sizes and examine whether there is any correlation between nanoparticle diameter and Ce(III) concentration. Another interesting experiment would be to examine particles synthesized in a pure oxygen environment versus a pure nitrogen environment. This may be a way of creating particles that possess varying Ce(III) concentrations but have similar properties, most importantly size and preferred crystal orientation. This would be helpful to further characterize the optical spectroscopy methods.

Polymers could also be added during synthesis to alter the normal synthesis process. The polymers could perform a number of rolls. They could coat the particles, acting to help repulse the particles and reduce aggregation. They could also be used to selectively coat the particles and the growth mechanisms, potentially altering their reactivity. If the polymer attached to the {111} plane, then the synthesis process would continue, but growth would be halted in the {111} plane, thus leaving the {100} plane to grow freely. This method could be used to grow selected structures, such as cubes, in which all exposed planes are {100}.

6.4 Dopants

Another aspect of the synthesis procedure that should be further examined is doping the ceria particles. Studies have shown that doping the particles with gold, gadolinium, or indium can increase their catalytic activity[44]. If proper dopants were identified, the optical spectroscopy methods could be used to characterize the new particles.

6.5 Oxidized Absorption Spectrum

When the hydrogen peroxide was used to oxidize the ceria, the absorbance spectra all had a higher value at 400 nm than before they were oxidized. Since this is the opposite effect than was expected, there is some phenomenon is going on that we have not been able to explain. This remains an enigma and future experimentation should be done to determine the source of these results.

References

1 A. Trovarelli. *Catal. Rev. Sci. Eng.* **38,** 1996, 439.
2 P. Patsalas, S. Logothetidis, L. Sygellou, and S. Kennou, *Phys. Rev. B* **68**, 2003, 035104.
3 T. Suzuki, I. Kosacki, H. Anderson and P. Colomban, *J. Am. Ceram. Soc.* **84**, 2001, 2007-14.
4 S. Tsunekawa, J.T. Wang and Y, Kawazoe, *J. Alloys and Compounds.* **408**, 2006, 1145-1148.
5 F. Zheng, S.W. Chan, J.E. Spanier, E. Apak, et. al., *Appl. Phys. Lett.* **80**, 2002.
6 T. Sakata and H. Mori, *Chem. Mater.* **9**, 1997, 2197-2204.
7 L. Tye and N. A. El-Masry, *Appl. Phys. Lett.* **65**, 3081, 1994.
8 B. Rzigalinski, *Tech. Canc. Resea. & Treatm.* **4,** 2005, 651-659.
9 D. Bailey, L. Chow, S. Merchant, S.C. Kuiry, et al., *Nat. Biotechnol.* **14**, 2003, 112.
10 B.A. Rzigalinski, K. Meehan, R.M. Davis, Y. Xu, W.C. Miles, C.A. Cohen. *Nanomedicine*, **4,** 2006, 399.
11 M.D. Sturge, *Phys. Rev.* **127**, 1962, 768-773.
12 F. Zhang, P. Wang, J. Koberstein, S. Khalid and S.-W. Chan, *Surf. Sci.* **563**, 2004, 74.
13 D.R. Mullins, S.H. Overbury, D.R. Huntley, *Surf. Sci.* **409**, 1998, 307.
14 J.E. Spanier, R.D. Robinson, F. Zheng, S.W. Chan and I.P. Herman, *Phys. Rev. B* **64,** 2001, 245407.
15 W.C. Miles, J. Clinton, K. Meehan, B.A. Rzigalinski, R.M Davis. *Journal TBD*
16 J.I. Pankove, *Optical Processes in Semiconductors*, Dover Publications, Inc. New York, 1971.
17 C.C. Davis, *Lasers and Electro-Optics*, Cambridge University Press, Cambridge, 1992.
18 E. Hecht, *Optics*, Addison Wesley, San Francisco, 2002.
19 A. Bokov, A. Chaudhuri, A. Richardson, *Mech. Ageing Dev.*, **125**, 2004, 811.
20 D. Harman, *Antioxid. Redox. Signal*, **5**, 2003, 557-561.
21 B. Halliwell, *J. Neurochem.* **97**, 2006, 1634-1658.
22 J. Rodrigo, A.P. Fernandez, J. Serrano, M.A. et. al., *Free Radic. Biol. Med.*, **39**, 2005, 26-50.
23 D.S. Warner, H. Sheng, I. Batinic-Haberle, *J. Exp. Biol.* **207**, 2004, 3221-3231.
24 M. Das, S. Patil, N. Bhargava, J. F. Kang, L. M. Riedel, S. Seal, J. J. Hickman, *Biomaterials*, **28**(11), 2007, 1918.
25 NanoActive Cerium Oxide, NanoScale Corporation, 2007.
26 Nanophase Cerium Oxide: Technologies and Capabilities, Romeoville, 2007.
27 H.I. Chen, H.Y. Chang, *Coll. and Surf.*, **242**, 2004, 61-69.
28 S. Basu, P.S. Devi and H.S. Maiti, *J. Mater. Res.*, **19**, 2004, 3162-3171.
29 L. Yin, Y. Wang, G. Pang, Y. Koltypin and A. Gedanken, *J. Coll. and Int. Sci.*, **246**, 2002, 78-84.
30 J. Zhang, S. Ohara, T. Adschiri, et. al., *Adv. Mater.*, **19**, 2007, 203-206.

31 M. Yamashita, K. Kameyama, S. Yabe, S. Yoshida, et. al., *J. Mater. Sci.*, **37,** 2002, 683-687.
32 Z.D. Dohcevic-Mitrovic, M. Grujic-Brojcin, M. Scepanovic, et. al., *J. of Phys.: Cond. Matt.*, **18**, 2006, 2061-2068.
33 N.V. Skorodumova, R. Ahuja, S.I. Simak, et. al., *Phys. Rev. B.*, **64**, 2001, 115108.
34 S. Tsunekawa, R. Sivamohan, S. Ito, A. Kasuya, and T. Fukuda, *Nanostruct. Mater.,* **11**(1), 1999, 141.
35 F. Esch, S. Fabris, L. Zhou, T. Montini, C. Africh, P. Fornasiero, G. Comelli, R. Rosei, *Science* **309**, 2005, 752-755.
36 S. Tsunekawa, S. Ito and Y. Kawazoe, *Appl. Phys. Lett.*, **85**, 2004, 3845-3847.
37 K. Zhou, X. Wang, X. Sun, Q. Peng and Y. Li, *J. Catal.*, **229**, 2005, 206-212.
38 Z.X. Yang, T.K. Woo, M. Baudin, K. Hermansson, *Journal of Chemical Physics* **120**, 2004, 7741-7749.
39 S. Deshpande, S. Patil, S. Kuchibhatla, S. Seal, *Applied Physics Letters,* **87,** 2005.
40 S. Tsunekawa, T. Fukuda, A. Kasuya, *Surface Science,* **457**, 2000, L437-L440.
41 L. Wu, H.J. Wiesmann, A.R. Moodenbaugh, et. al., *Phys. Rev. B*, **69,** 2004, 125415.
42 H.I. Chen, H.Y. Chang, *Ceram. Int.*, 2005.
43 S.K. Kim, U. Paik, S.G. Oh, et. al., *Jpn. J. Appl. Phys.*, **42**, 2003, 1227-1230.
44 Q. Fu, W. Deng, H. Saltsburg, M. Flytzani-Stephanopoulos, *Appl. Catal. B.*, **56**, 2005, 57-68.

Appendix A

Absorbance Plots of Ceria Samples at an adjusted pH

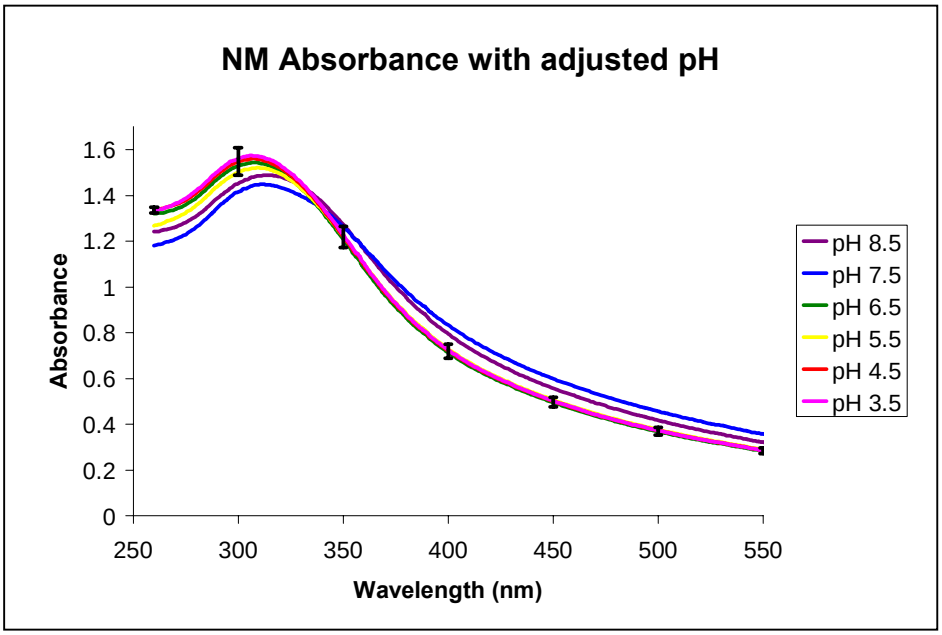

Figure 29. Absorbance spectra of NM with adjusted pH.

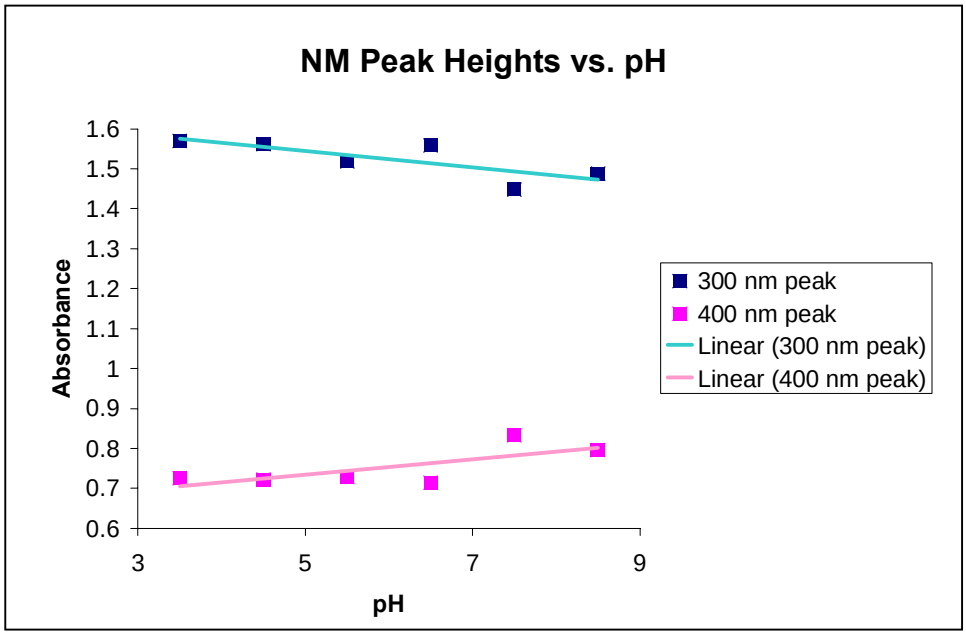

Figure 30. Values of 300 nm peak and 400 nm peak versus pH for N160.

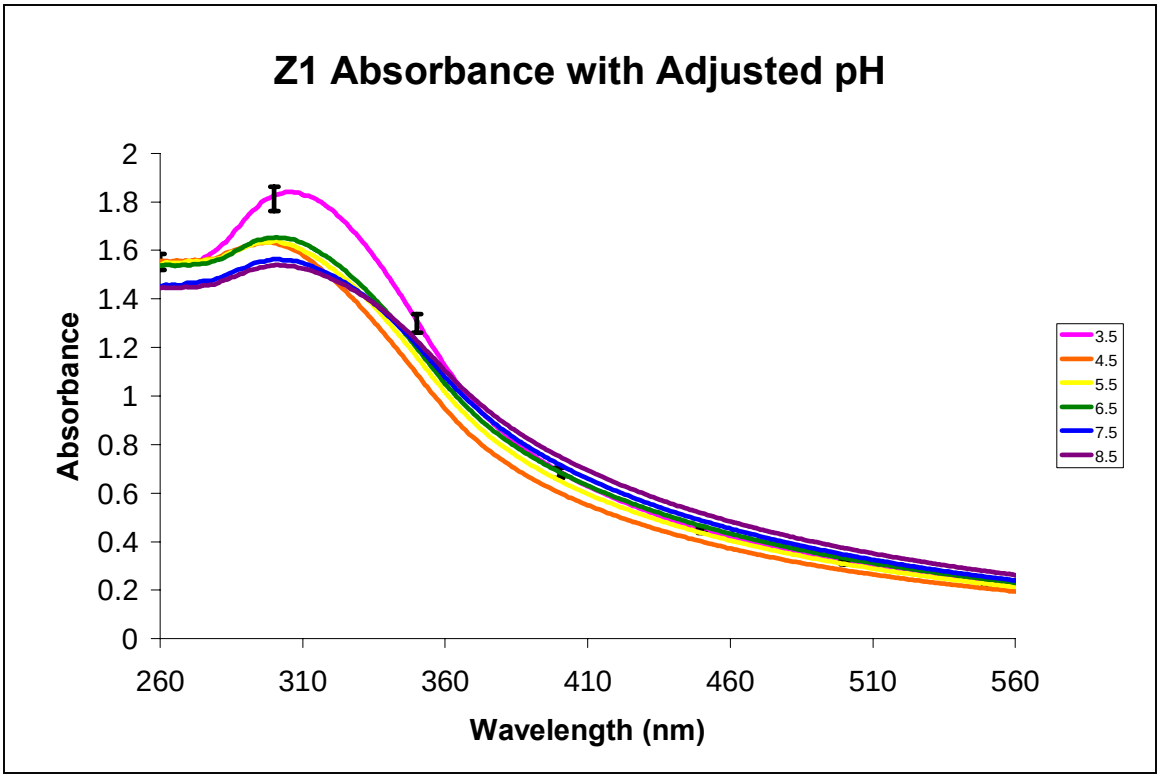

Figure 31. Absorbance spectra of Z1 with adjusted pH.

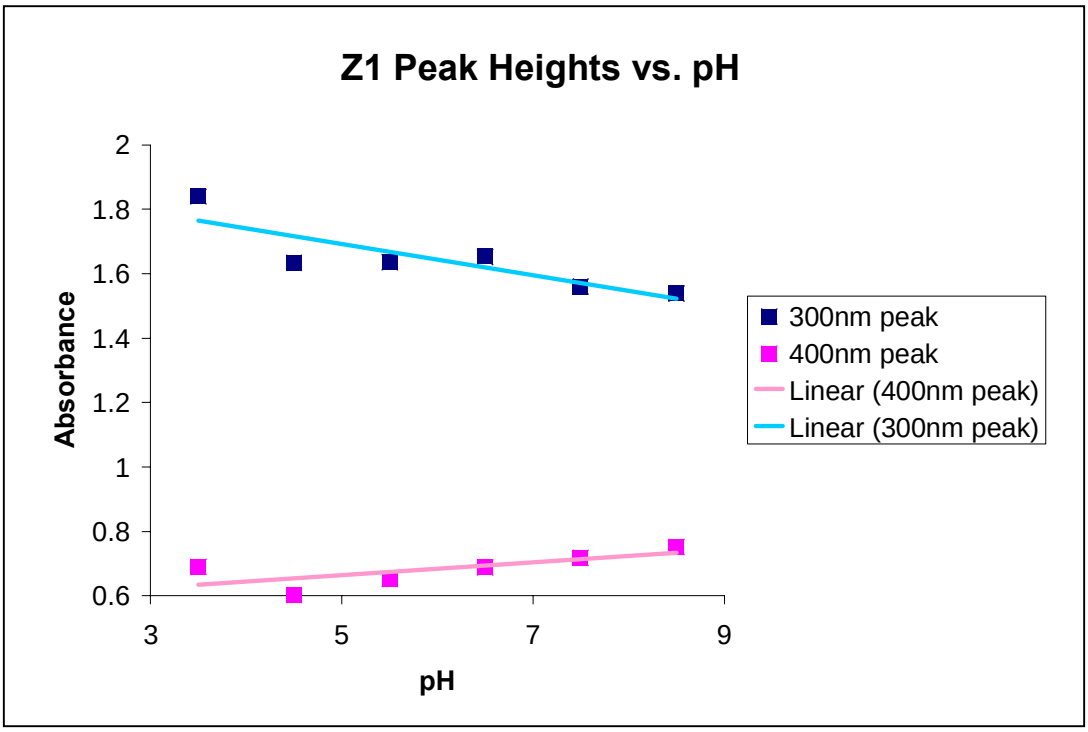

Figure 32. Values of 300 nm peak and 400 nm peak versus pH for Z1.

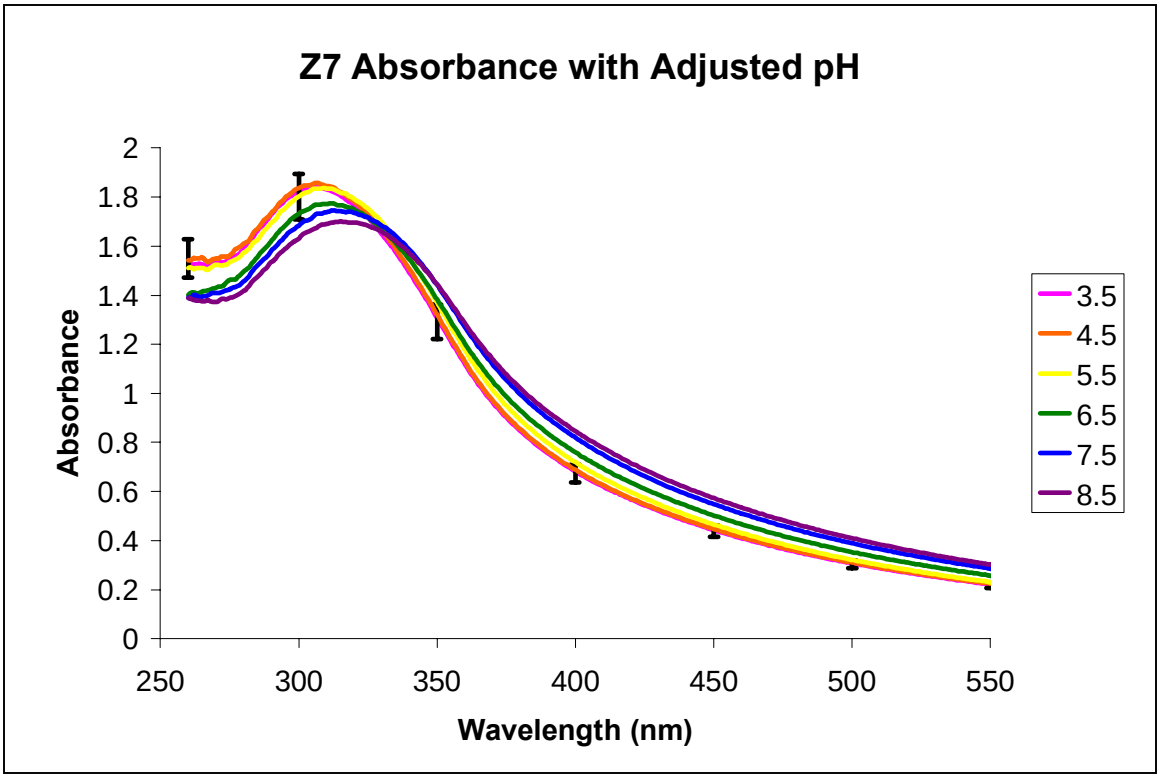

Figure 33. Absorbance spectra of Z7 with adjusted pH.

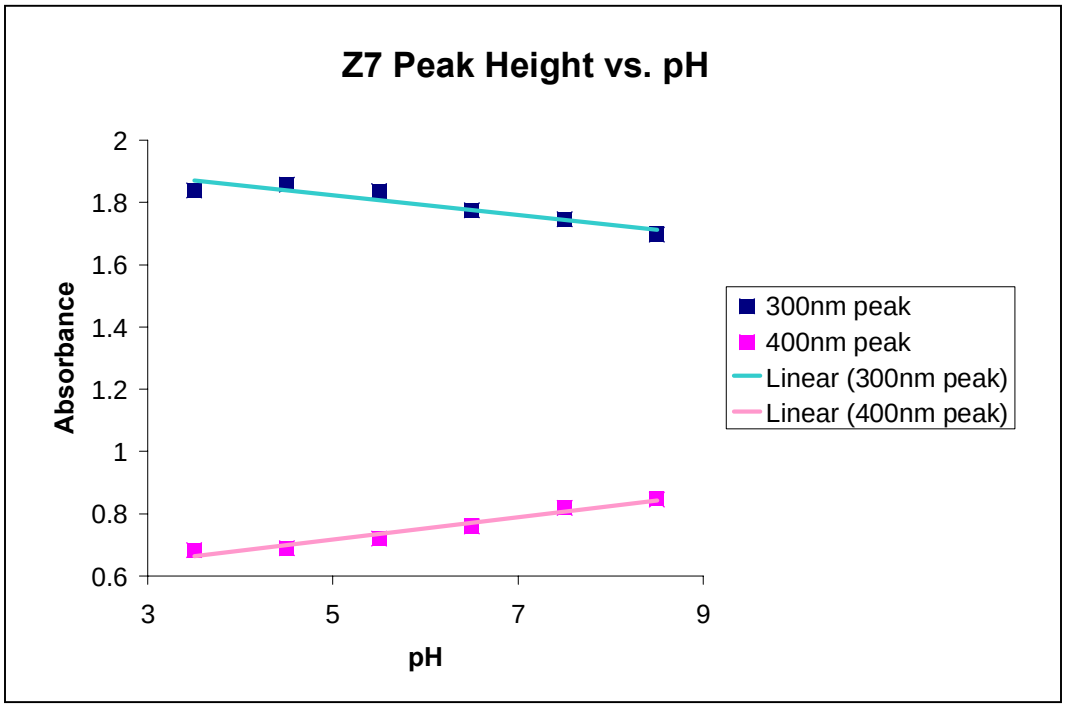

Figure 34. Values of 300 nm peak and 400 nm peak versus pH for Z7.

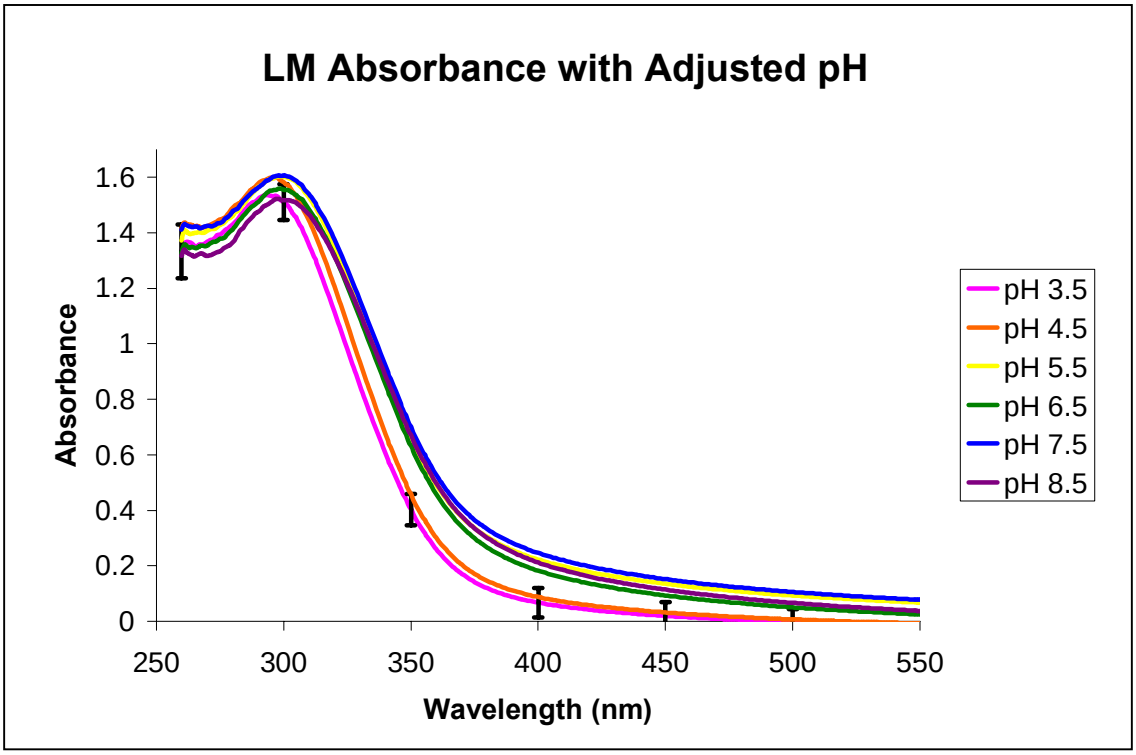

Figure 35. Absorbance spectra of LM with adjusted pH.

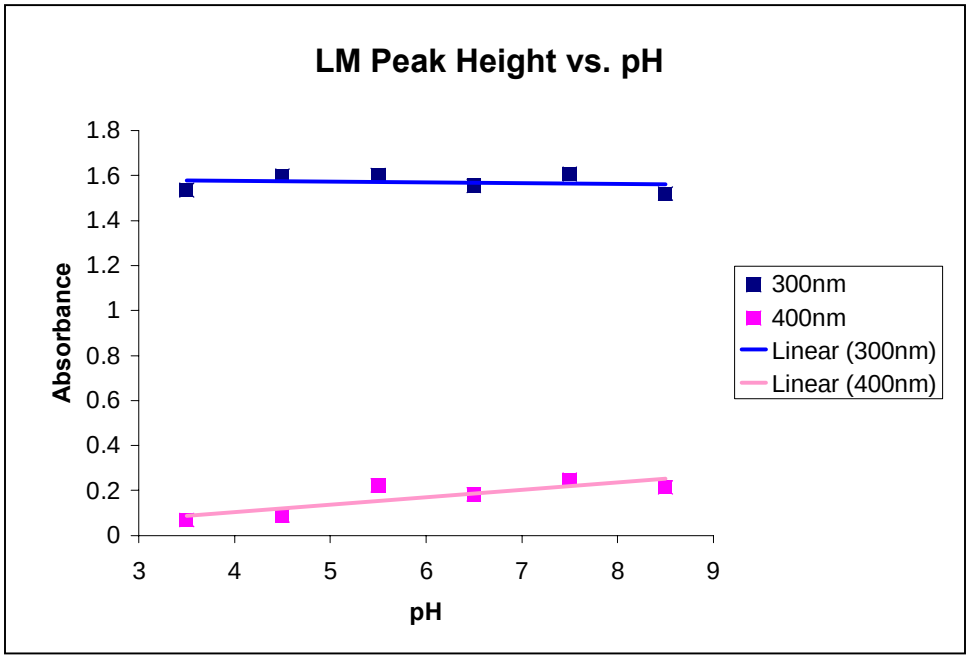

Figure 36. Values of 300 nm peak and 400 nm peak versus pH for N160.

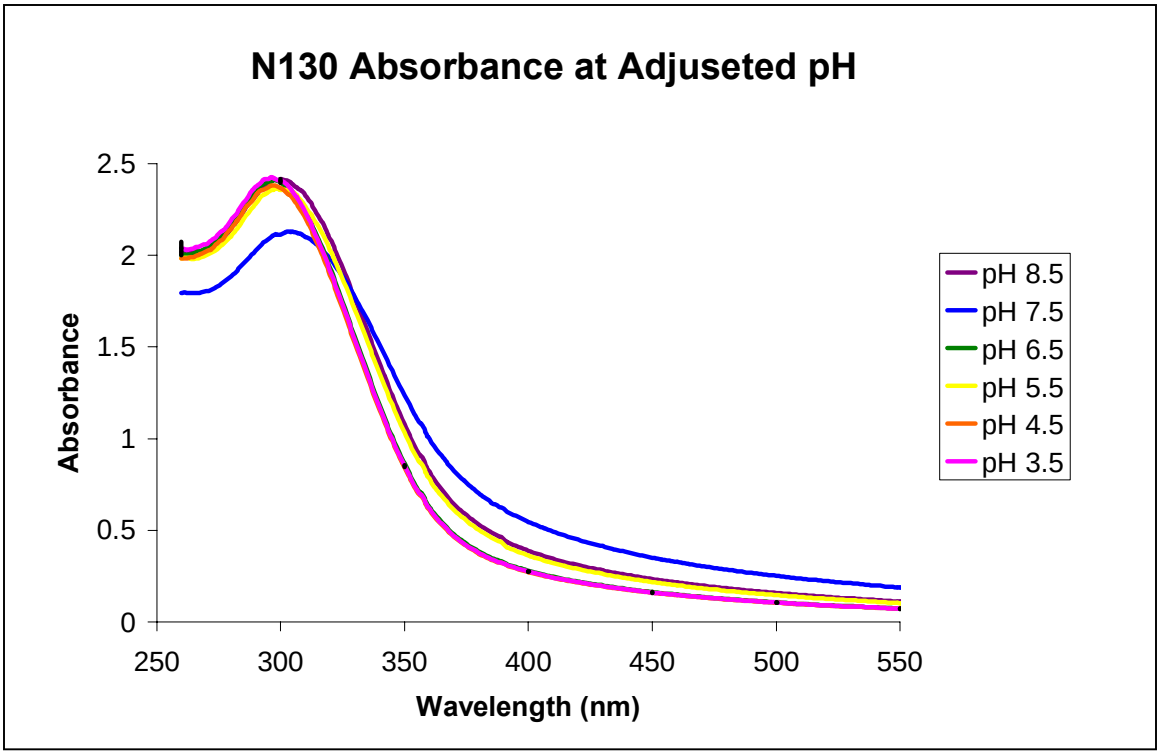

Figure 37. Absorbance spectra of N130 with adjusted pH.

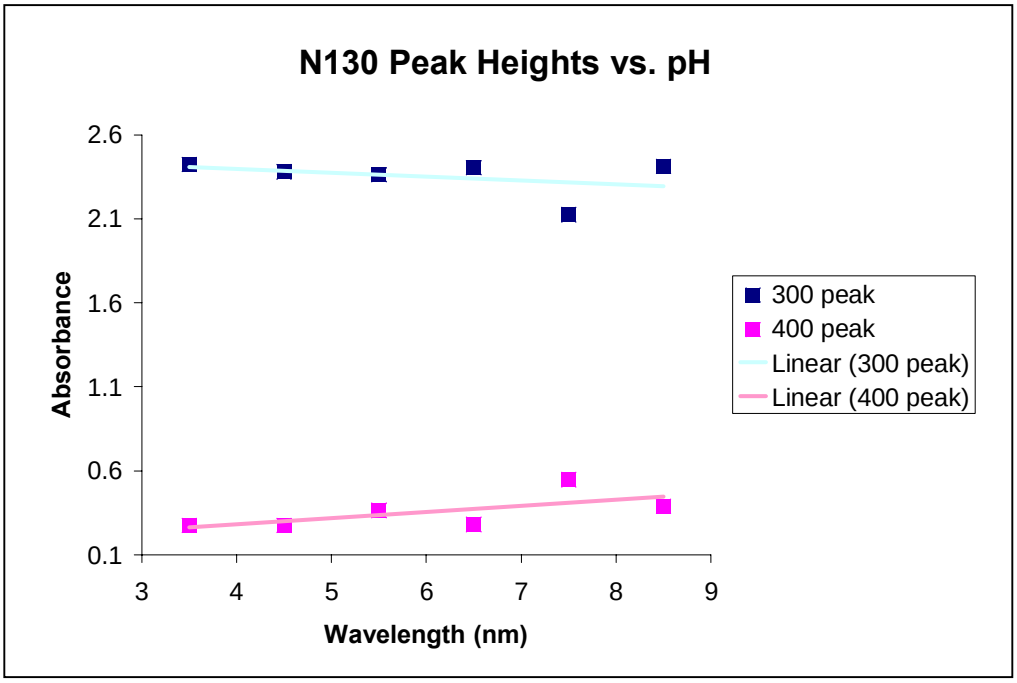

Figure 38. Values of 300 nm peak and 400 nm peak versus pH for N130.

Appendix B

Absorbance Plots of Oxidized and Unoxidized Ceria Samples

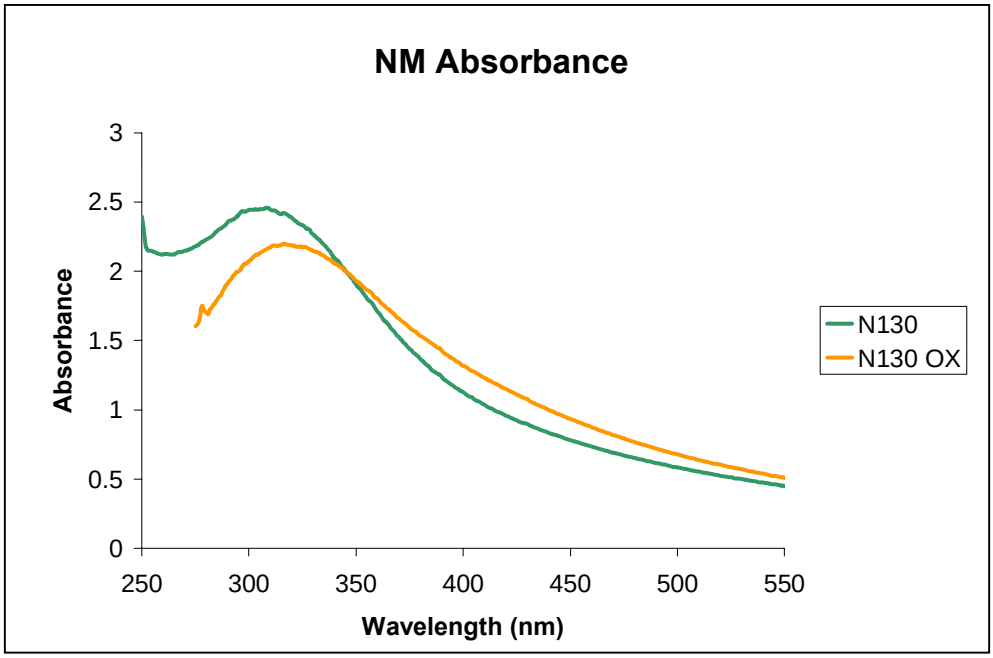

Figure 39. Absorbance spectra of NM before and after being oxidized.

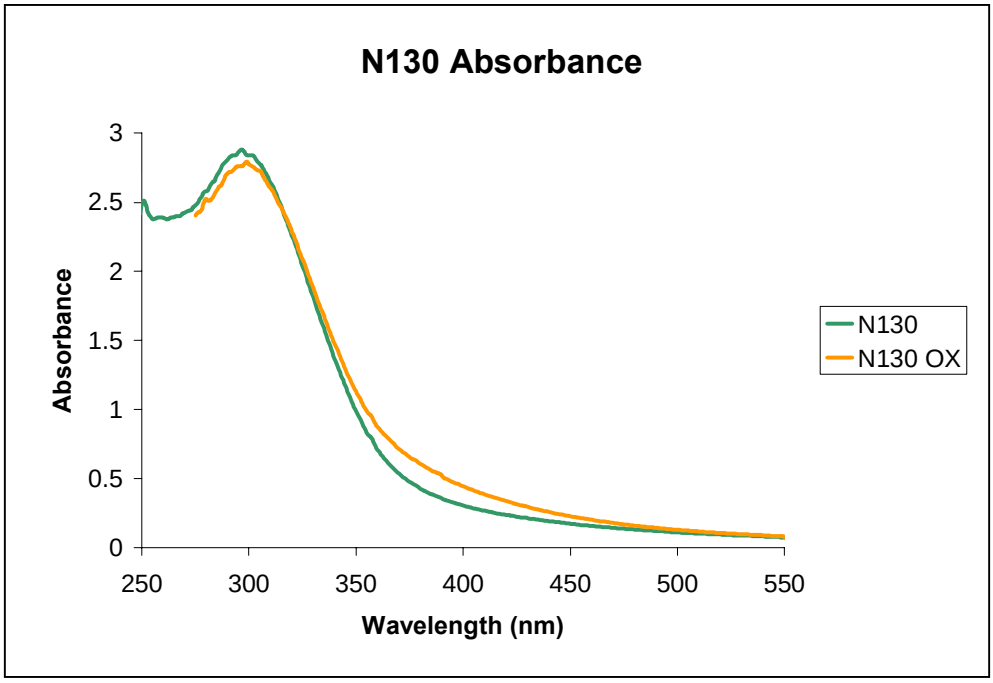

Figure 40. Absorbance spectra of N130 before and after being oxidized.

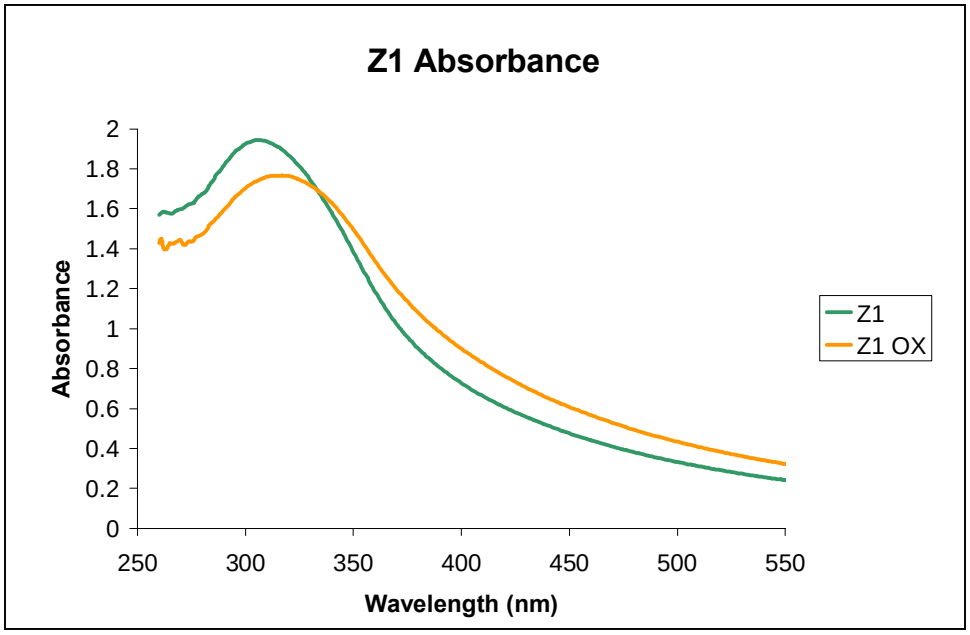

Figure 41. Absorbance spectra of Z1 before and after being oxidized.

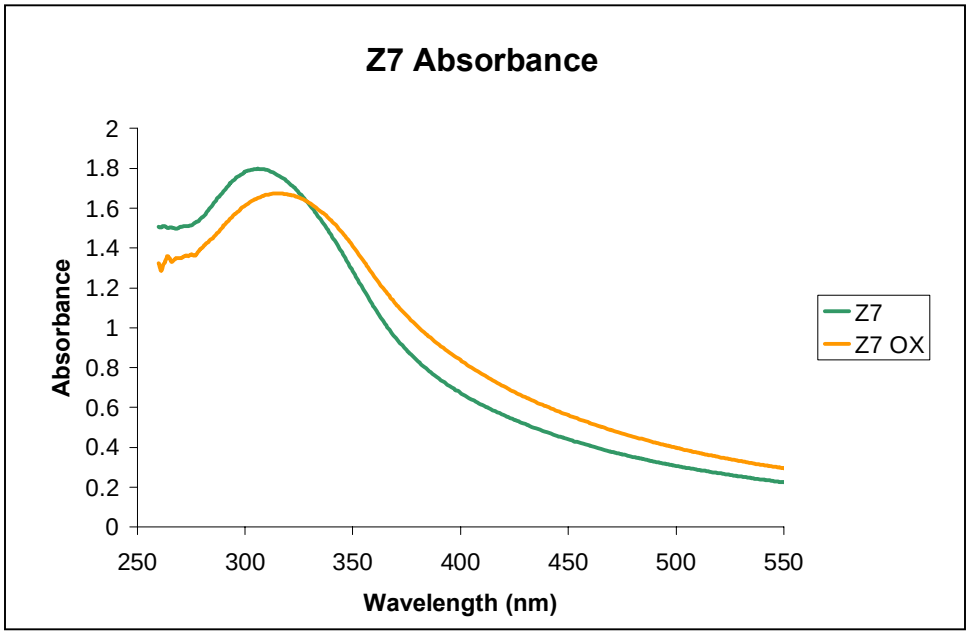

Figure 42. Absorbance spectra of Z7 before and after being oxidized.

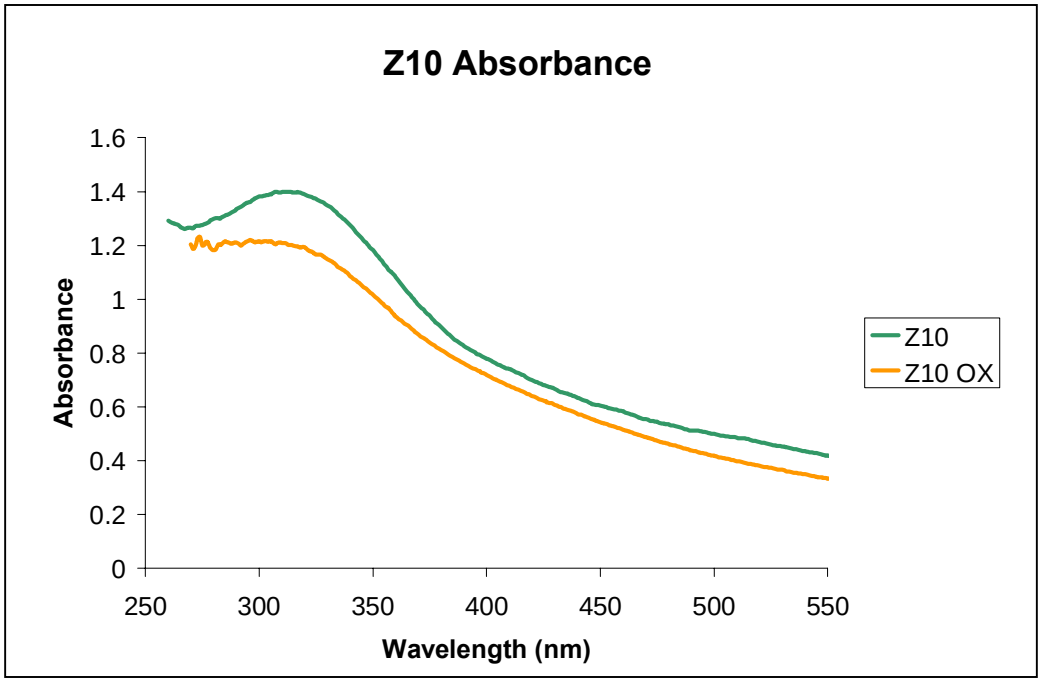

Figure 43. Absorbance spectra of Z10 before and after being oxidized.

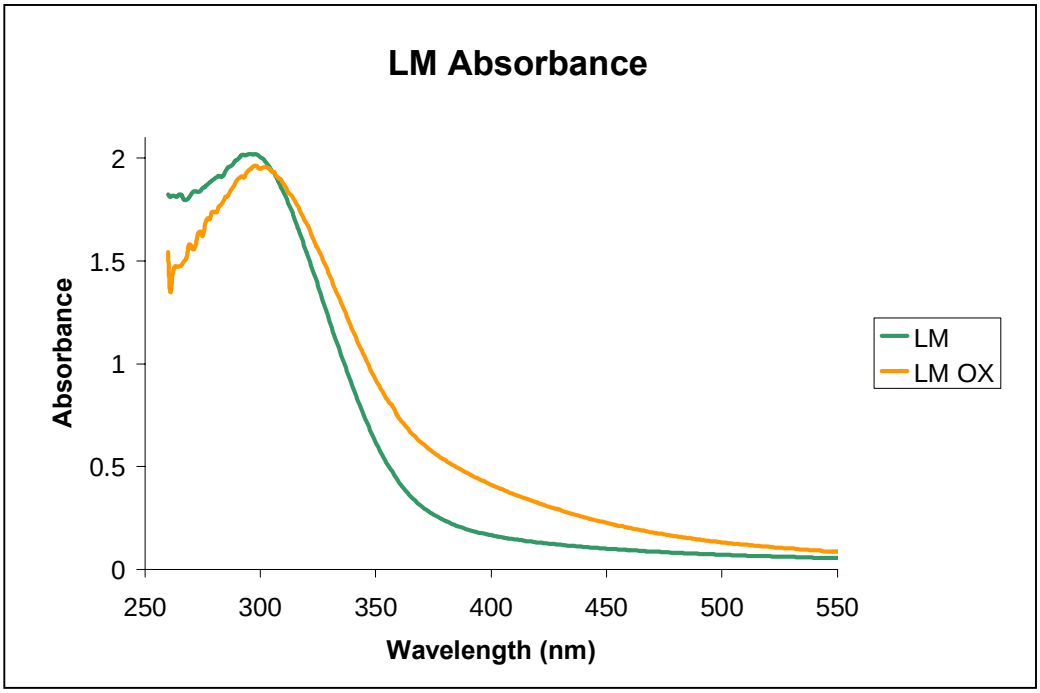

Figure 44. Absorbance spectra of LM before and after being oxidized.

Appendix C

Fluorescence and Excitation Spectra for Ceria Samples

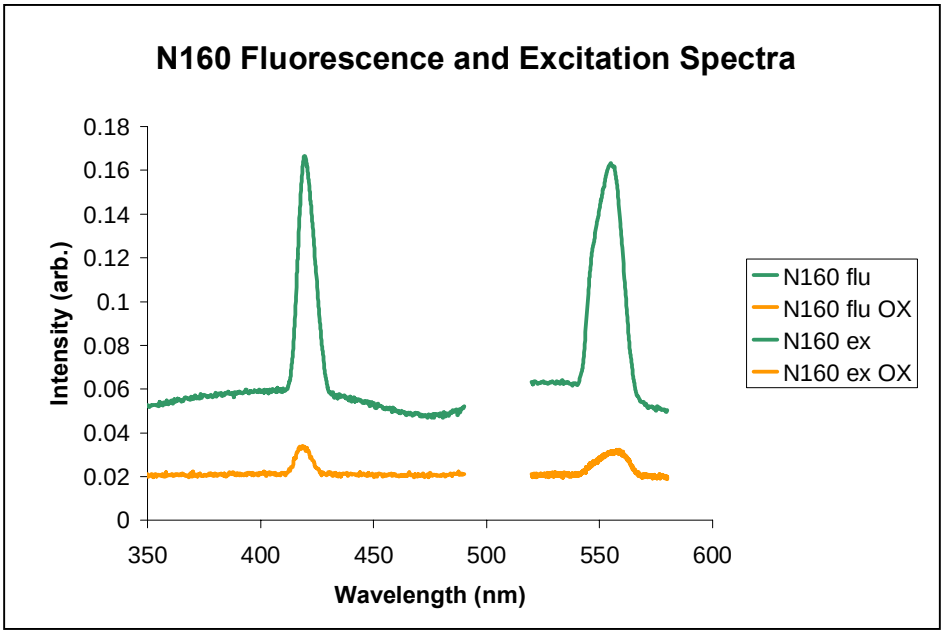

Figure 45 Fluorescence and excitation scan of N160 before and after oxidation.

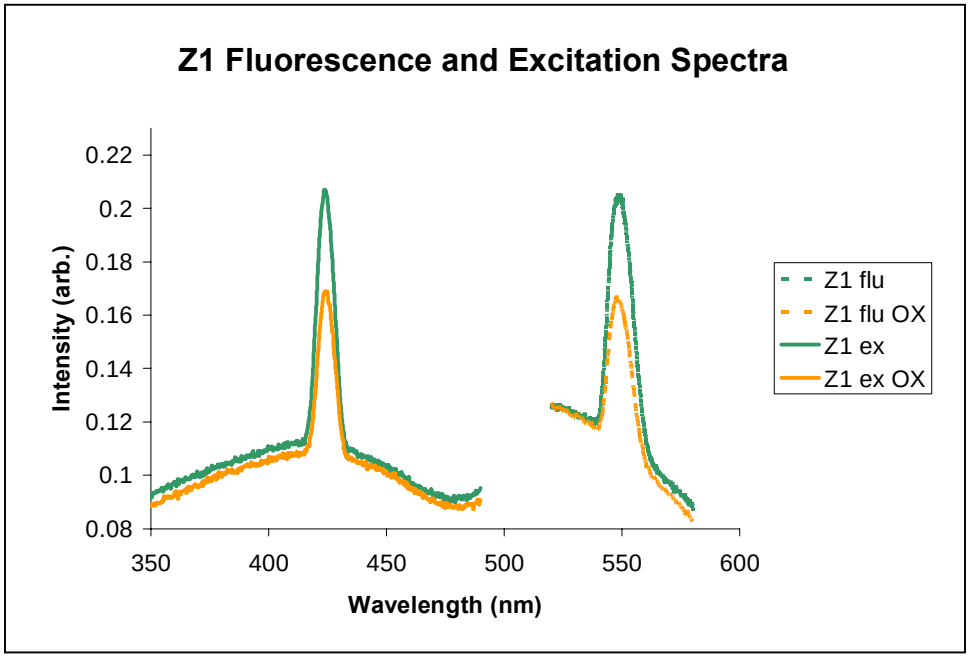

Figure 46 Fluorescence and excitation scan of Z1 before and after oxidation.

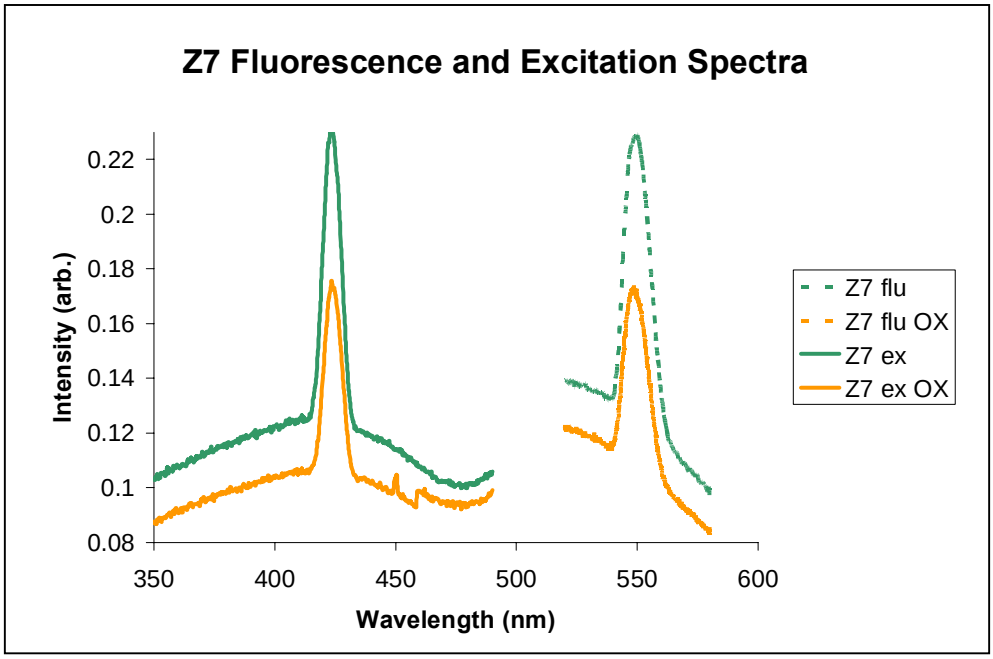

Figure 47 Fluorescence and excitation scan of Z7 before and after oxidation.

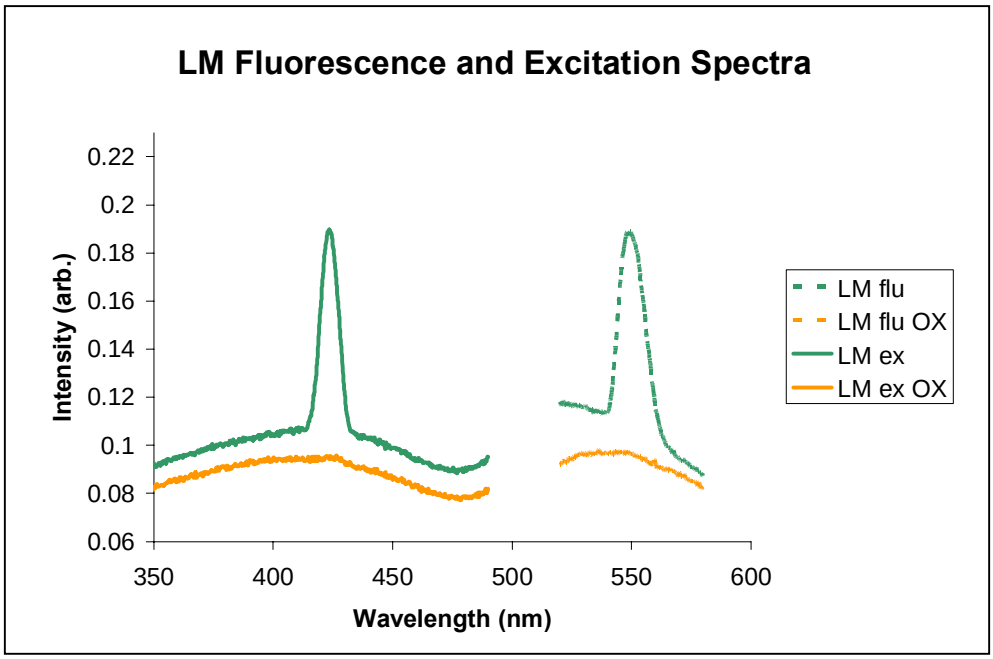

Figure 48 Fluorescence and excitation scan of LM before and after oxidation.

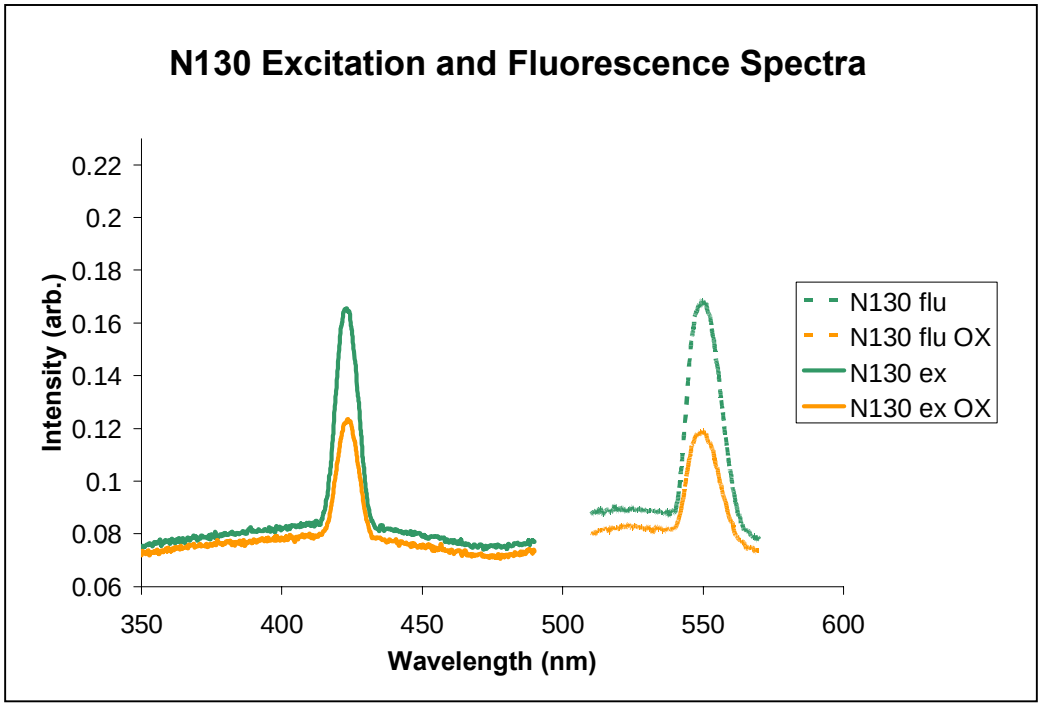

Figure 49 Fluorescence and excitation scan of N130 before and after oxidation.

Appendix D

XPS Spectra for Ceria Samples

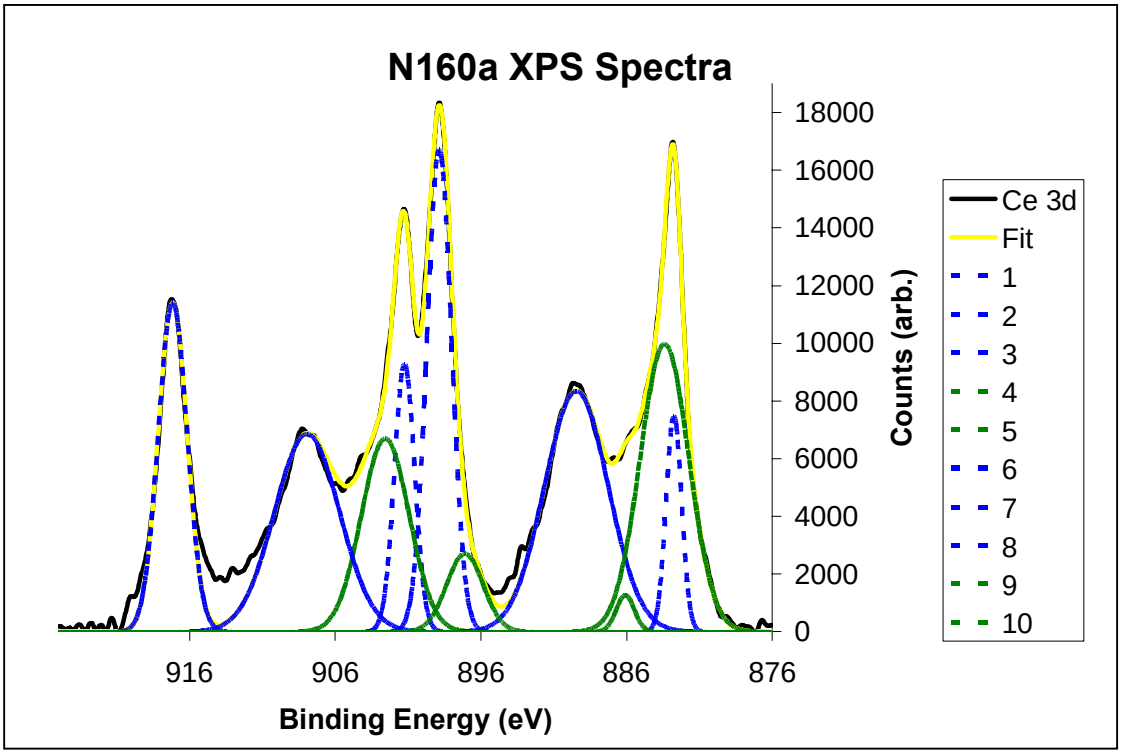

Figure 50. Measured and fitted XPS spectra of N160a along with ten Gaussian peaks.

Table 6. Gaussian peak parameters for XPS spectrum of N160a. N160a had an EMS value of 10.12.

#	Area	Area%	Position	Intensity	FWHM
1	6690	4.00%	882.76	4988	1.26
2	23725	14.00%	898.86	11144	2
3	10744	6.40%	901.24	6192	1.63
4	1307	0.80%	886.09	847	1.45
5	18290	10.80%	902.56	4463	3.85
6	18796	11.10%	917.15	7611	2.32
7	30383	18.00%	889.45	5564	5.13
8	25502	15.10%	907.93	4572	5.24
9	27811	16.50%	883.4	6648	3.93
10	5639	3.30%	897.1	1802	2.94

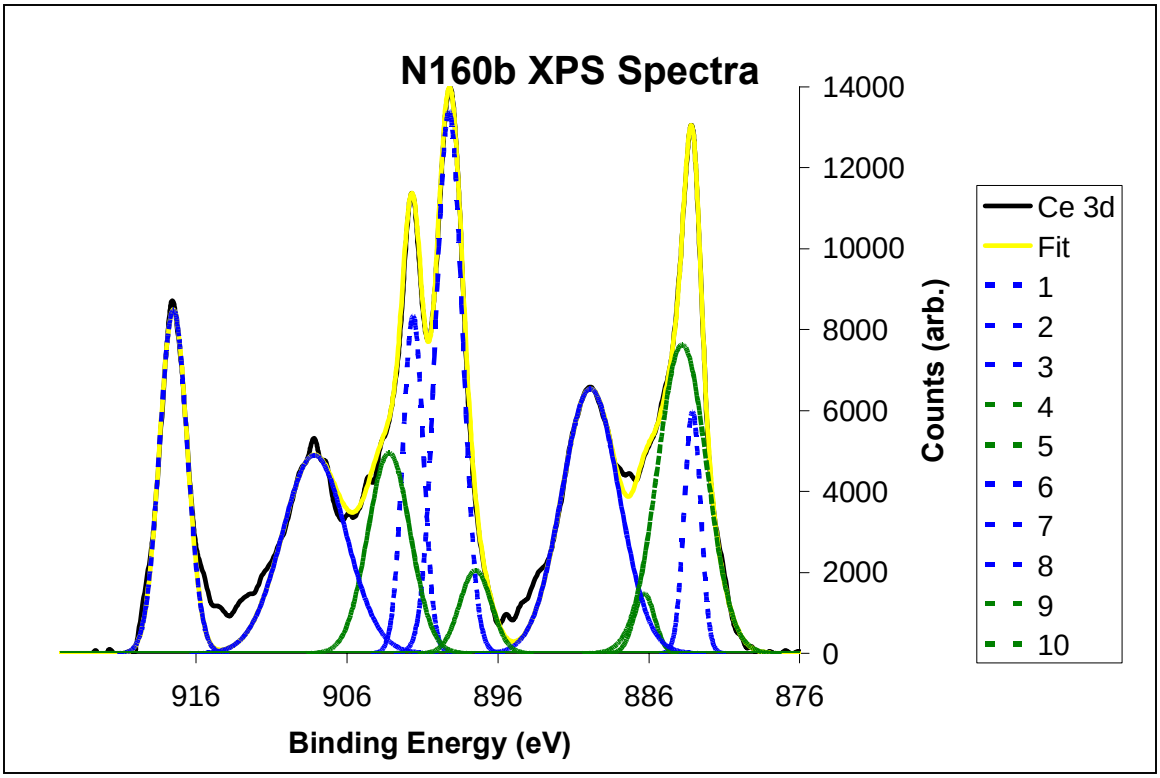

Figure 51. Measured and fitted XPS spectra of N160b along with ten Gaussian peaks.

Table 7. Gaussian peak parameters for XPS spectrum of N160b. N160b had an EMS value of 6.55.

#	Area	Area%	Position	Intensity	FWHM
1	5423	4.40%	883.1	3980	1.28
2	19761	16.00%	899.23	8925	2.08
3	9464	7.70%	901.61	5557	1.6
4	1676	1.40%	886.3	984	1.6
5	11603	9.40%	903.2	3303	3.3
6	12951	10.50%	917.49	5659	2.15
7	20773	16.90%	889.86	4356	4.48
8	17238	14.00%	908.16	3265	4.96
9	20781	16.90%	883.78	5084	3.84
10	3553	2.90%	897.47	1368	2.44

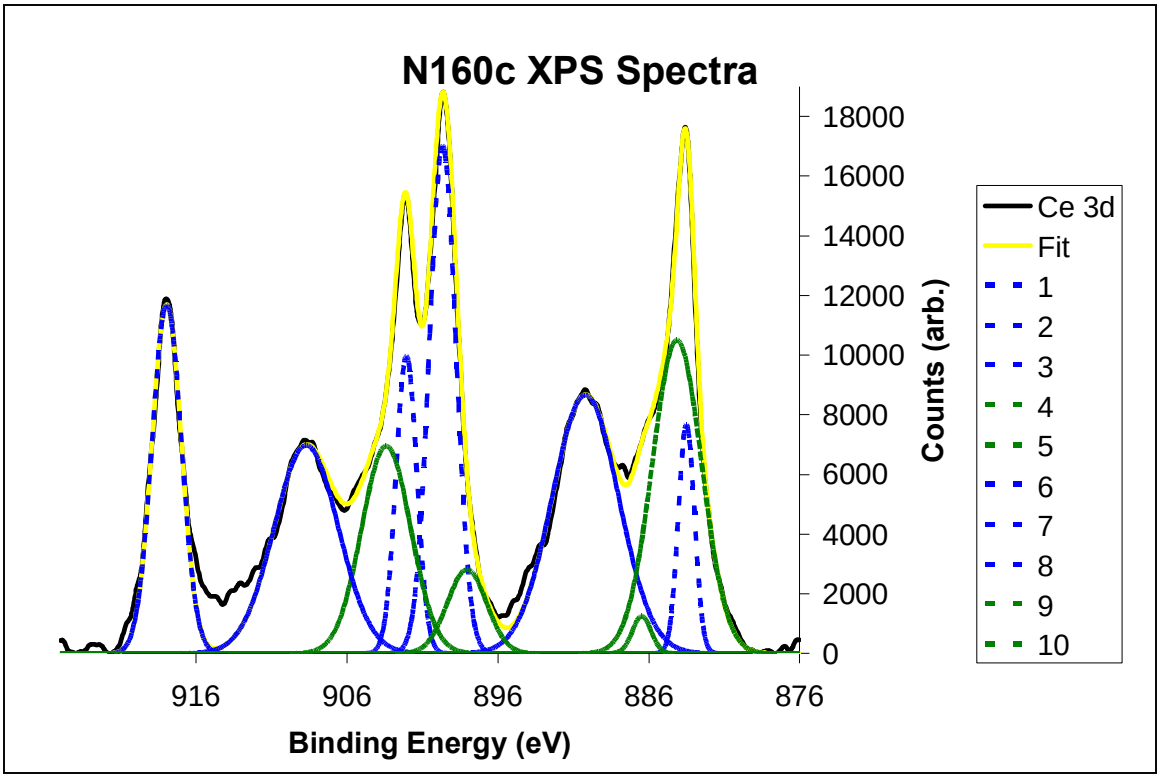

Figure 52. Measured and fitted XPS spectra of N160c along with ten Gaussian peaks.

Table 8. Gaussian peak parameters for XPS spectrum of N160c. N160c had an EMS value of 10.59.

#	Area	Area%	Position	Intensity	FWHM
1	6863	3.90%	883.5	5117	1.26
2	25134	14.50%	899.65	11352	2.08
3	11478	6.60%	902.05	6656	1.62
4	1287	0.70%	886.46	834	1.45
5	18810	10.80%	903.39	4638	3.81
6	19006	10.90%	917.93	7797	2.29
7	31804	18.30%	890.19	5779	5.17
8	24715	14.20%	908.69	4653	4.99
9	28696	16.50%	884.13	7002	3.85
10	6067	3.50%	898.04	1875	3.04

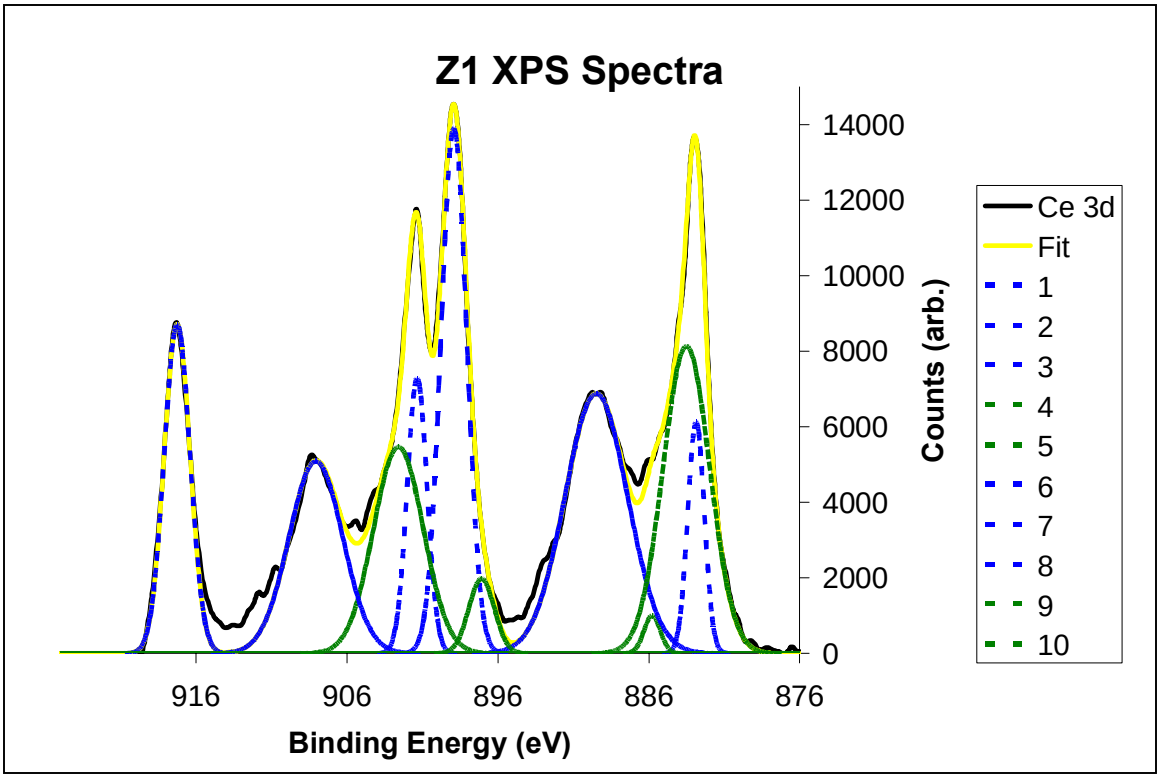

Figure 53. Measured and fitted XPS spectra of Z1 along with ten Gaussian peaks.

Table 9. Gaussian peak parameters for XPS spectrum of Z1. Z1 had an EMS value of 6.05.

#	Area	Area%	Position	Intensity	FWHM
1	5656	4.50%	882.86	4087	1.3
2	19840	15.90%	898.91	9273	2.01
3	8017	6.40%	901.34	4859	1.55
4	897	0.70%	885.77	669	1.26
5	14999	12.10%	902.58	3641	3.87
6	12422	10.00%	917.24	5806	2.01
7	23779	19.10%	889.47	4587	4.87
8	15052	12.10%	908.05	3391	4.17
9	21001	16.90%	883.5	5420	3.64
10	2762	2.20%	897.07	1317	1.97

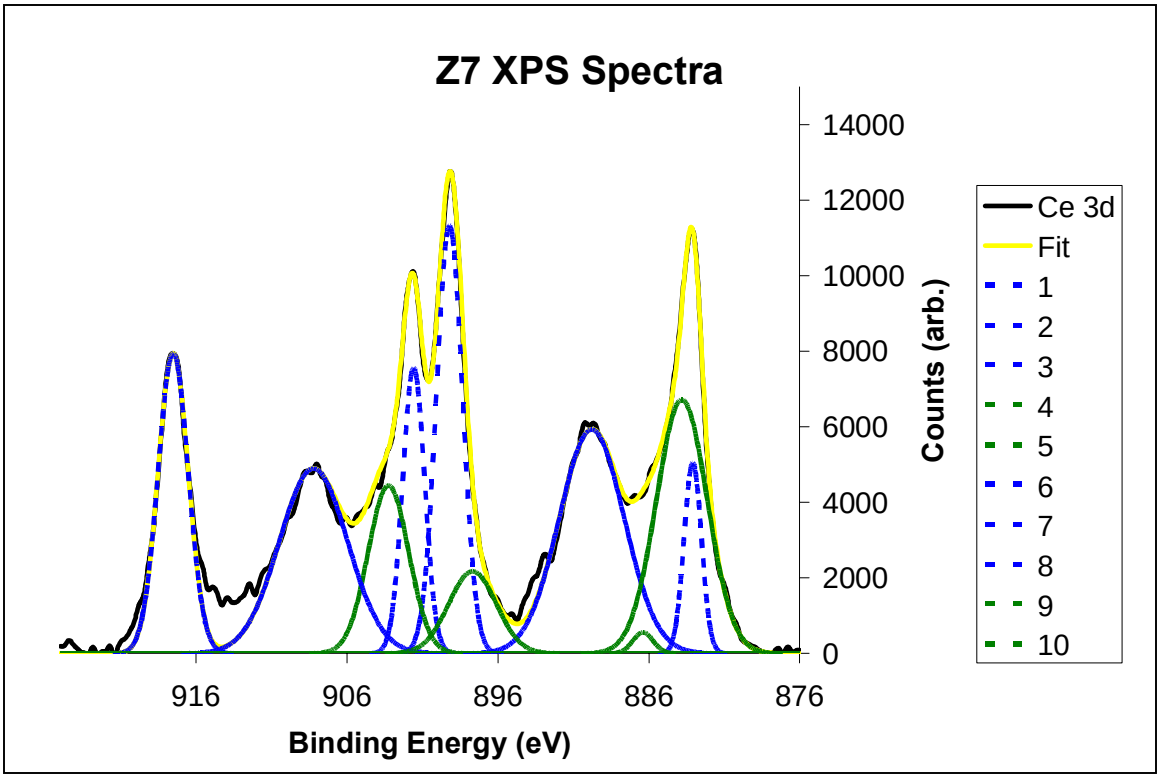

Figure 54. Measured and fitted XPS spectra of Z7 along with ten Gaussian peaks.

Table 10. Gaussian peak parameters for XPS spectrum of Z7. Z7 had an EMS value of 7.58.

#	Area	Area%	Position	Intensity	FWHM
1	4866	4.10%	883.08	3361	1.36
2	16397	13.80%	899.2	7551	2.04
3	9174	7.70%	901.57	5040	1.71
4	612	0.50%	886.38	371	1.55
5	9928	8.40%	903.24	2961	3.15
6	13253	11.20%	917.5	5298	2.35
7	21233	17.90%	889.77	3950	5.05
8	18432	15.60%	908.21	3261	5.31
9	18863	15.90%	883.8	4475	3.96
10	5695	4.80%	897.67	1446	3.7

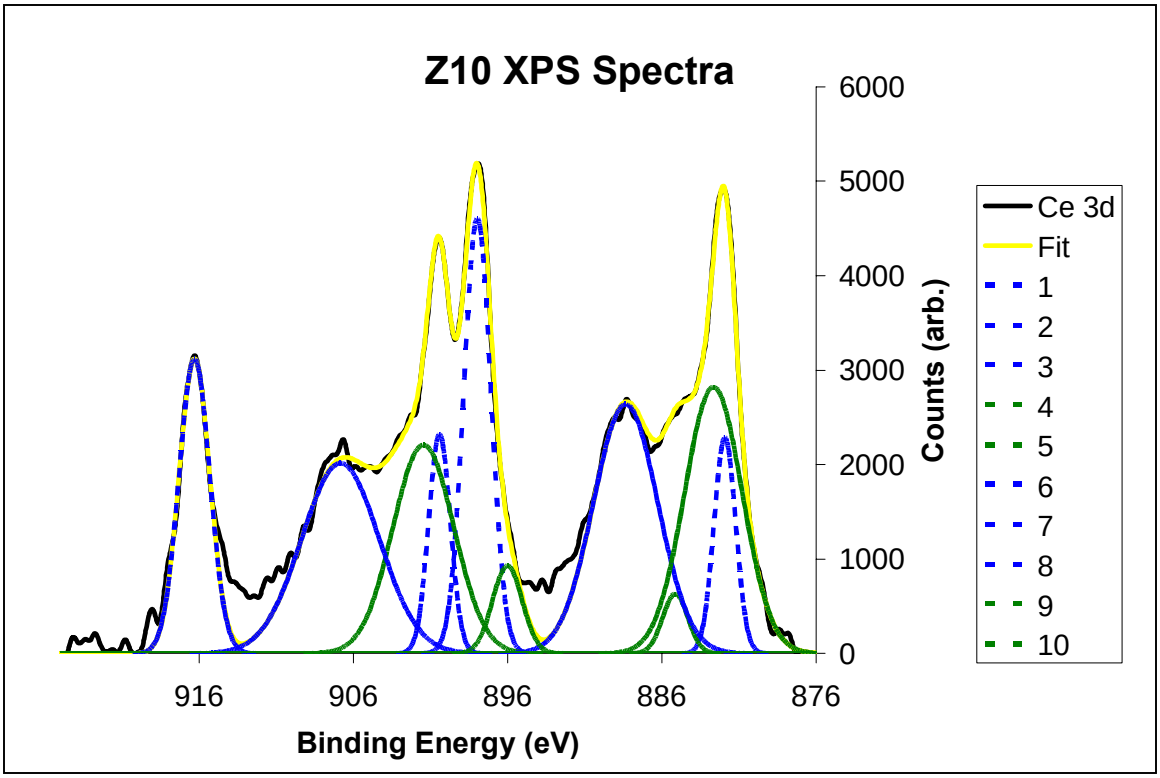

Figure 55. Measured and fitted XPS spectra of Z10 along with ten Gaussian peaks.

Table 11. Gaussian peak parameters for XPS spectrum of Z10. Z10 had an EMS value of 6.10.

#	Area	Area%	Position	Intensity	FWHM
1	2680	5.00%	881.92	1526	1.65
2	6767	12.70%	897.96	3071	2.07
3	2719	5.10%	900.41	1548	1.65
4	851	1.60%	885.13	421	1.9
5	7260	13.60%	901.45	1473	4.63
6	5181	9.70%	916.29	2080	2.34
7	9156	17.20%	888.35	1759	4.89
8	8414	15.80%	906.83	1342	5.89
9	8765	16.50%	882.66	1880	4.38
10	1480	2.80%	896.01	618	2.25

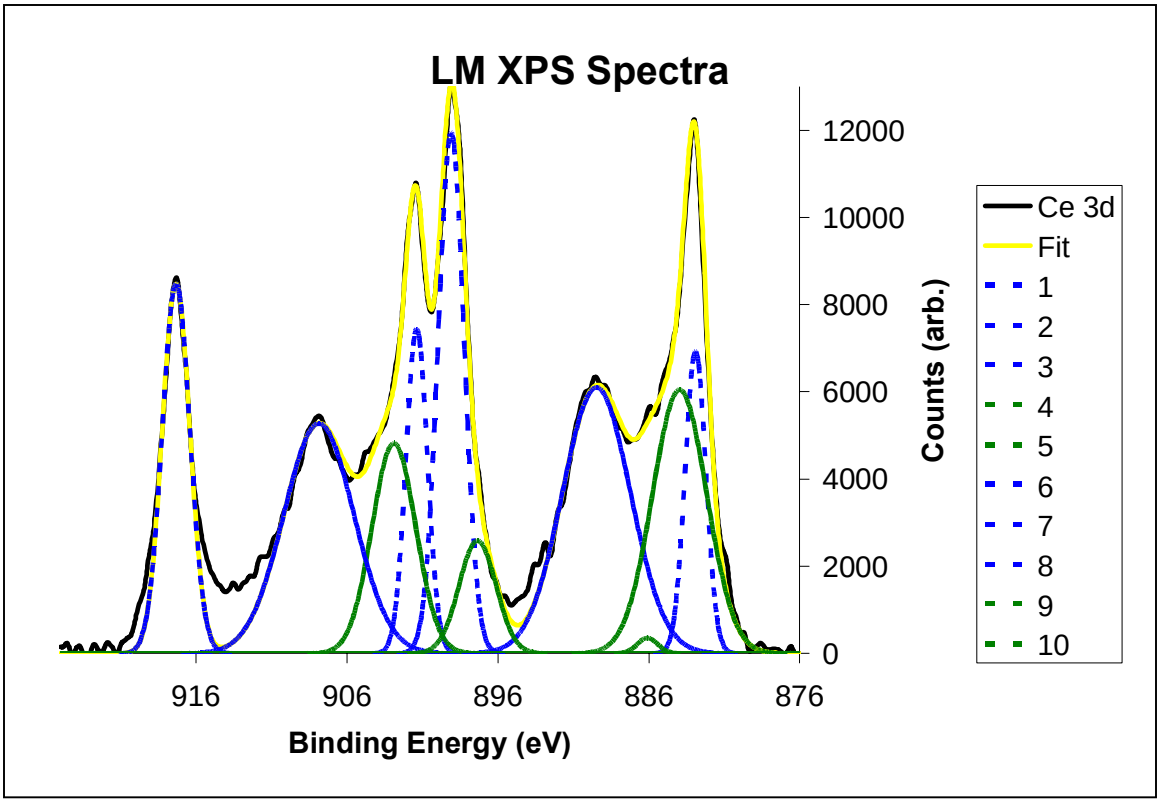

Figure 56. Measured and fitted XPS spectra of LM along with ten Gaussian peaks.

Table 12. Gaussian peak parameters for XPS spectrum of LM. LM had an EMS value of 11.19.

#	Area	Area%	Position	Intensity	FWHM
1	7963	6.30%	882.9	4618	1.62
2	17131	13.60%	899.09	7967	2.02
3	8823	7.00%	901.37	4963	1.67
4	393	0.30%	886.08	235	1.57
5	11625	9.30%	902.88	3212	3.4
6	12942	10.30%	917.31	5655	2.15
7	22901	18.20%	889.46	4067	5.29
8	20392	16.20%	907.85	3515	5.45
9	18103	14.40%	883.95	4030	4.22
10	5258	4.20%	897.34	1721	2.87

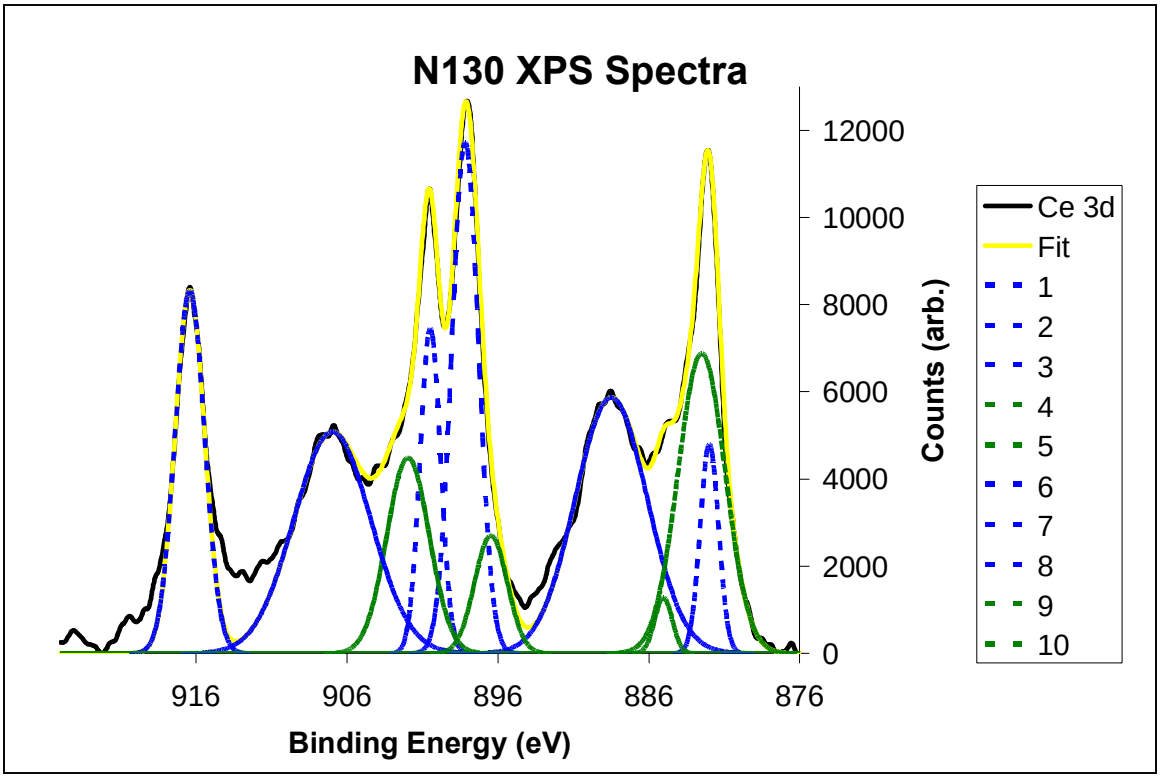

Figure 57. Measured and fitted XPS spectra of N130 along with ten Gaussian peaks.

Table 13. Gaussian peak parameters for XPS spectrum of N130. N130 had an EMS value of 13.80.

#	Area	Area%	Position	Intensity	FWHM
1	4900	4.00%	881.98	3197	1.44
2	17321	14.00%	898.16	7823	2.08
3	8417	6.80%	900.47	4973	1.59
4	1229	1.00%	885.02	849	1.36
5	10503	8.50%	901.94	2990	3.3
6	13590	11.00%	916.4	5551	2.3
7	23325	18.90%	888.48	3913	5.6
8	21566	17.40%	906.96	3388	5.98
9	17927	14.50%	882.49	4589	3.67
10	4831	3.90%	896.45	1801	2.52